Mechanics of Seashell Growth: Examining the relationship between incompatibility, shape, and internal stress

by

Dylan Carberry

B.S., Rensselaer Polytechnic Institute (2016)

Submitted to the Department of Mechanical Engineering
in partial fulfillment of the requirements for the degree of

Master of Science in Mechanical Engineering

at the

MASSACHUSETTS INSTITUTE OF TECHNOLOGY

June 2023

Authored by: Dylan Carberry
Department of Mechanical Engineering
May 18, 2023

Certified by: Tal Cohen
Associate Professor
Thesis Supervisor

Accepted by: Nicolas Hadjiconstantinou
Chairman, Department Committee on Graduate Theses

Mechanics of Seashell Growth: Examining the relationship between incompatibility, shape, and internal stress

by

Dylan Carberry

Submitted to the Department of Mechanical Engineering
on May 18, 2023, in partial fulfillment of the
requirements for the degree of
Master of Science in Mechanical Engineering

Abstract

Seashells are a fascinating example of surface growth in nature. As they develop, both their macroscopic form and their internal microstructure evolve, with the latter transitioning between different layer sizes and orientations during the shell's growth process. Several studies have examined the morphogenesis of seashells, with some considering the kinematics of growth that lead to different eventual shapes, and others investigating the biochemical pathways of these processes. However, the role of internal mechanical stresses that may develop due to incompatibility has yet to be investigated. In this thesis, we present a framework that models the shell growth continuously, with an aim to investigate the role of internal stresses on the structural changes that have been reported to occur within seashells. Considering an axisymmetric growing body and accounting for surface growth as an arbitrary sequence of addition of incompatible circular rings on its outer perimeter, we study the shape and mechanical forces that can develop throughout the shell's growth. Our findings show that incompatibility has a large impact on the shape of a shell during surface growth, especially during early stages of development. This influence may be crucial in explaining the recorded crystallographic reorientation that is typical to various seashells.

Thesis Supervisor: Tal Cohen
Title: Associate Professor

Acknowledgments

I would first like to thank my advisor, Professor Tal Cohen, for teaching me to be a graduate level researcher. I am deeply appreciative of Tal supporting me throughout my transition from industry to academia, taking my mechanical intuition and molding it into a skillset that was able to perform the research required for this degree. I am honored to call myself a member and now an alumni of Tal Cohen's Nonlinear Solid Mechanics Group.

I would also like to thank my fellow group members, Hudson Borja da Rocha, Chockalingam Senthilnathan, Hannah Varner, Xuanhe Li, Brendan Unikewicz, and Joseph Bonavia for all of their assistance during my time at MIT. I am grateful for their unique ability to transition between providing astute technical advice and criticism on my tougher research problems, to then supplying countless laughs and reprieves from my day-to-day workload. I would like to thank all the graduate professors (Rohan Abeyaratne, Lallit Anand, Christina Chase, and Anette Hosoi among others) and teaching assistants in my classes these past two years for creating an environment that encouraged collaboration and innovation.

I would like to thank Igor Zlotnikov and Richard Johannes Best of the Technische Universität Dresden for providing the inspiration to study the mechanics of the shell growth. I am appreciative of the kindness and patience they displayed while I learned the ropes of being a theoretical mechanician. Outside of academia, I would like to thank Reid Almand, Adam Rellinger, and Josh Rellinger for their mentorship during my employment at Honda and for recommending me for this degree.

Finally, I would like to thank my parents, MaryAnn and Jim, and my partner, Kelsey, for taking such great care of me. I am endlessly grateful for the innumerable hours they spent listening to me expound on seashells, and for their unconditional love during the ebbs and flows of graduate school at MIT.

Contents

List of Figures

Chapter 1

Introduction

The phenomenon of growth is ubiquitous in our daily life. Growth can take many forms and works across scales of both time and size. It impacts numerous processes such as cell mitosis, seed germination, the growth of plants, and the development of a human from child to adult. Growth has been studied by individuals across cultures and disciplines, including philosophers, artists, and scientists [14]. It enables organisms to react to their environment throughout their lifetime, often adjusting in order to improve their chances at survival in a given setting.

For most of the 20^{th} century, the problem of understanding growth was primarily explored by the field of biology. However, in the last forty years with the rise of biophysics and biomedical engineering, the problem of describing and understanding growth quantitatively has branched into other scientific disciplines [14]. Growth has become a large focus in the field of mechanics, in particular as researchers have attempted to measure the effect that mechanical forces and stress have on influencing the development of living things [26].

The evidence that mechanical loading has a direct impact on growth is seen all over our world. Figure 1-1 shows some examples of this behavior. The shape of the outer shell of a red-eared slider turtle is largely altered when constrained by a plastic six-pack ring [21]. The growth of a tomato inside a box results in a cubic tomato due to the loading from the confinement affecting the fruit's final shape [22]. NASA has shown that the reduced gravity in space causes astronauts to lose bone density during

prolonged flights [41, 18, 36]. Trees adapt to their surroundings during their growth process, spreading their roots to minimize the mechanical loading of a constraining concrete sidewalk [29, 11].

(a) Growth-induced shape change of the shell of a female red-eared slider turtle [21] (Credit: [28]).

(b) Tomato grown inside a cuboidal box confinement. This practice has the potential to reduce fruit storage and transportation costs. [22] (Credit: Flickr/moonimage).

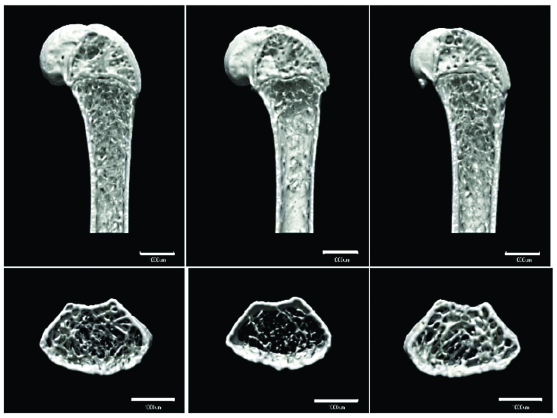

(c) Impact of gravity on bone density of astronauts on internation space station [18]

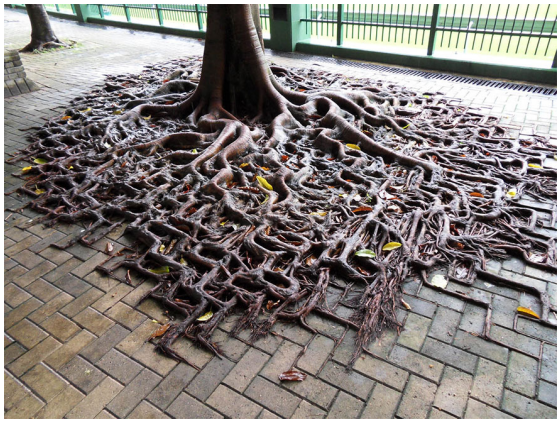

(d) Tree roots growing through sidewalk grooves (Credit: imgur/worldbeyondyourown)

Figure 1-1: Examples of growth impacted by mechanical forces.

1.1 Seashells

Seashells are another biological system whose growth is impacted by the presence of mechanical forces. They come in a wide variety of shapes and sizes, but are often composed of simple patterns (Figure 1-2). The history of the growth process is recorded in the shape of the shell due to the long time scale over which the shell grows.

Most seashells come from mollusks, a large group of marine animals that includes clams, mussels, and oysters, which emit shells as a protective covering. Mollusks are the third largest phyla of animals in nature (trailing insects and worms), consisting of over 110,000 estimated species [7]. Shells that originate from mollusks are excreted from the outer surface of the animal and are made up of mostly calcium carbonate [33]. As the mollusk ages, the shell gets larger and more calcium carbonate is exuded from the mantle. After death, the produced shell remains [16].

(a) Diversity and variability of shells originating from mollusks on display at the Berlin Natural History Museum (Image Credit: LoKiLeCh/ Wikimedia).

(b) Assorted limpet seashells displaying axisymmetry (Image credit: Tango22/ Wikimedia).

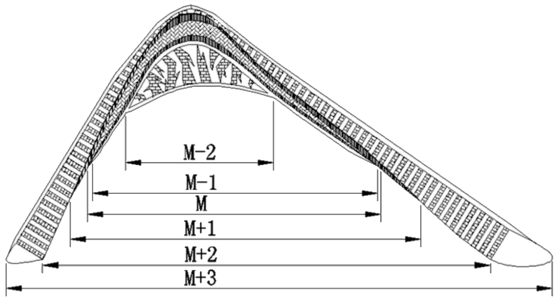

(c) Schematic drawing of the cross-section of a limpet seashell with labeled layers, created by cutting from the shell's apex. (Image Credit: [44]).

Figure 1-2: Variety of seashells originating from mollusks.

Although the shapes and patterns of seashells have been extensively studied and

applied, the underlying growth process has received comparatively less exploration. Seminal studies in the field of seashell growth have been conducted by Moulton et. al [25, 26, 9, 8]. Their research introduced a mathematical framework [25] that considers surface growth and explores the ornamental patterns on shells in three-dimensional space [26, 9]. They also investigated the coiling of shells produced by snails [8]. While their model describes the growth kinematics in three dimensions with continuous growth velocities, its kinetics are limited to local energy arguments. The shape evolution of the system is represented by discretizing the growth of the shell, modeling it as the addition of inextensible rods connected to a rigid material through a bed of springs. Consequently, the model only accounts for local mechanical forces.

Several researchers have utilized scanning electron microscopes (SEMs) to observe the fractured cross-sections of seashells and analyze their internal structure [5, 31, 32, 47, 45]. As seen in Figure 1-3, some seashells display a change in internal structure throughout their development, with the layers of the shell transitioning between different sizes and orientations [31, 45] as they elongate. Several factors could explain these changes to the crystallography of the shell during growth. This reorientation of layers could be controlled by biophysics [39, 40] or prescribed mineralization of the shell [17]. The internal stress associated with shell growth also could be a potential cause of the material internal structure reorientation seen in shells. A model that fully captures the mechanical forces associated with shell growth is needed to correctly attribute internal stresses as the cause of this structure change.

Our research objective is the development a thermodynamically consistent and continuous growth model that integrates the kinematics and kinetics of seashell growth. This model comprehensively captures the intricate shape and internal stresses involved in the growth process of a seashell, and sheds light on the phenomenon of crystallographic reorientation. This model accounts for both the global and local mechanical forces acting during shell growth. In this thesis, we focus on modeling the kinematics of the shell using arbitrary kinematic inputs, laying the foundation for future coupling with a continuum kinetic law. We first simplify the kinematics of the shell by assuming axisymmetry, enabling the development of a continuum model

for the kinetics. To investigate the ability of kinematics alone to capture the internal structural changes of a seashell, we perform an energy minimization analysis over the shell's growth period.

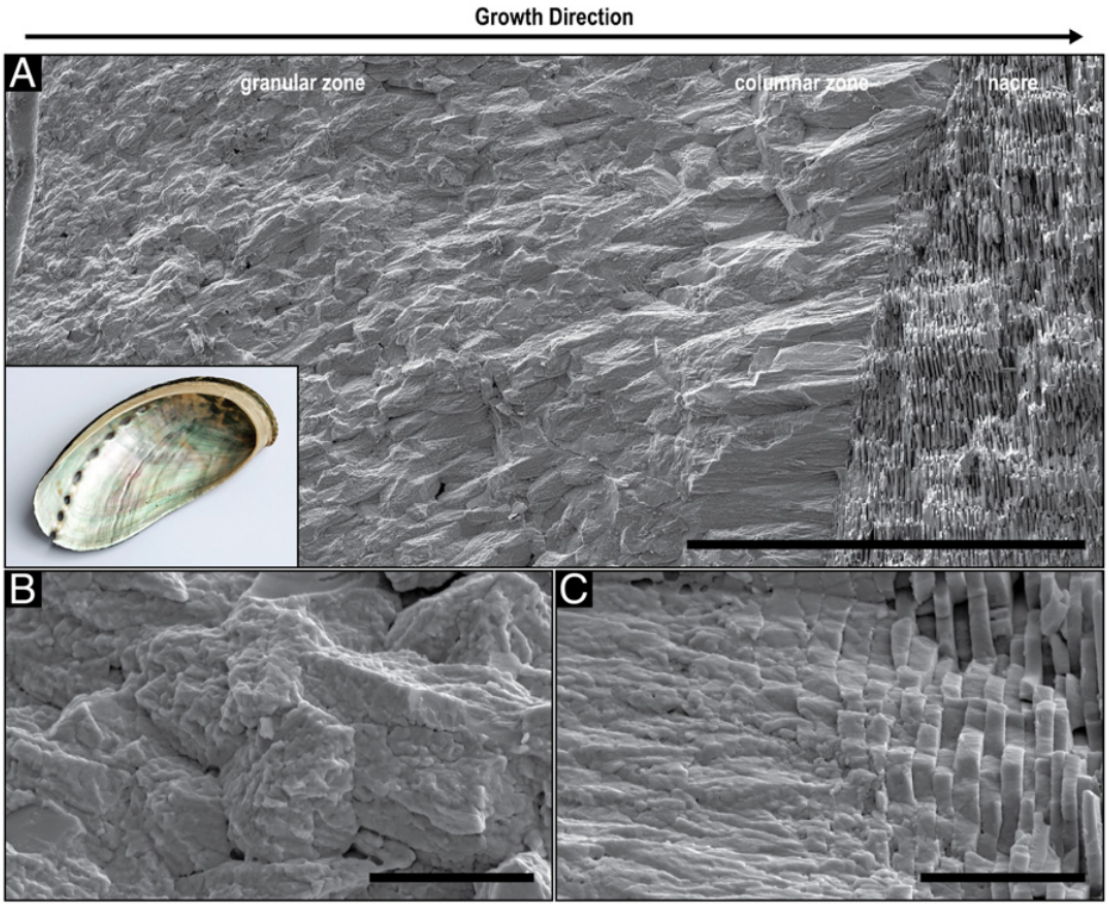

Figure 1-3: Structural analysis of the *Haliotis asinina* shell. (A) SEM image of fractured shell shows transition between granular, columnar and nacreous layers (Scale bar, 50 µm.) (B) Higher magnification of the central region of the granular layer. (Scale bar, 5 µm.) (C) Higher magnification of the columnar–nacre transition. (Scale bar, 5 µm.) [31].

1.2 Growth Studies

To model the growth of seashells and to investigate the effect of mechanical forces on the system, we need to further categorize existing approaches to modeling growth.

1.2.1 Volumetric Growth

In the field of mechanics, growth is divided into two categories: volumetric growth and surface growth [27]. Volumetric growth occurs through an addition of volume throughout the body due to a mass source. The set of material points is usually unchanged through this growth process while each material point can change its volume. The kinematics of volumetric growth were first described using continuum mechanics by Skalak et. al. in the early 1980s [35, 2]. This work described growth in a 3-D finite strain setting using a volumetric growth tensor denoted by $\mathbf{F}_g$. This growth tensor acted in a similar manner to the typical deformation gradient $\mathbf{F}$ in finite elasticity, in that the growth tensor described the growth between two points in time much like the deformation gradient depicts the strain between two configurations of a body [2].

1.2.2 Incompatibility

If a body grows uniformly and in the absence of external constraints, then no internal stresses are generated and we can consider the growth to be compatible. However, if the growth is nonuniform, or subjected to external constraints, it may be incompatible, thus inducing an internal strain field and corresponding internal stresses [30]. Incompatible growth is typically modeled using a multiplicative decomposition of the deformation gradient $\mathbf{F}$ [37, 38, 23, 23, 13, 15, 3]. This tensor is decomposed into a growth part $\mathbf{F}_g$ and an elastic part $\mathbf{F}_e$ where $\mathbf{F} = \mathbf{F}_e\mathbf{F}_g$ [2]. As shown in Figure 1-4, the growth tensor $\mathbf{F}_g$ describes the mapping of a body from its real and compatible reference configuration Ω_0, to an imaginary configuration that is not physically attained, where the cells within the body have undergone different amounts of growth and are incompatible with one another. The elastic deformation tensor $\mathbf{F}_e$ then maps the deformation from this imaginary incompatible configuration to the final deformed configuration of the body Ω that is physically attained [21]. This incompatible growth generates residual stresses that can, in turn, affect the future growth of the system itself.

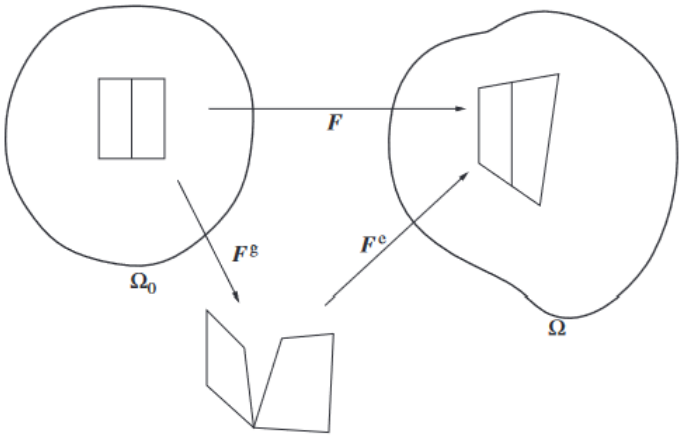

Figure 1-4: Multiplicative decomposition of the deformation gradient $\mathbf{F}$ for incompatible growth into growth $\mathbf{F_g}$ and elastic $\mathbf{F_e}$ parts [2].

1.2.3 Surface Growth

Surface growth happens due to the proliferation of mass at the boundary or edge of the body. Unlike volumetric growth, this addition of material results in the introduction of new material points to the body. Skalak and collaborators extended their studies of kinematics of volumetric growth to the case of surface growth by accounting for the addition of material points between physically attained configurations of the body and by defining both surface and growth velocities [34]. Many studies have shown that surface growth of a body can be affected by the accumulation of stress and the history of the construction of the body. These processes include plants [4][12], planetary formation [6][19][20], sand-pile growth [42] and additive manufacturing [46]. Importantly, this has also been shown to be true in our system of interest, the seashell, where the elongation of a lathe is best modeled by the addition of material at its outermost boundary. Chirat et. al. (2021) have shown that ammonites twist their shape and break symmetry to relax the built up residual stresses generated by the surface growth mismatch between the secreted shell tube and the symmetric body of the organism [8].

1.3 Problem Statement

We have now characterized the seashell as a system that is experiencing surface growth and have identified incompatibility and the associated residual stresses as potential causes of the crystallographic reorientation seen in these shells. The overarching goal for this research project, as discussed in Section 1.1, is to create a continious and thermodynamically consistent growth model for the seashell, to help investigate the impact of internal stresses on the structural changes that occur within seashells. For the scope of this thesis, we focus on outlining the framework of this growth model with an arbitrary kinematic input controlling the amount of incompatibility in the system. Our goal is to explore the following questions:

1. How does incompatibility influence the shape of shell surface growth?
2. For a given incompatibility, what are the internal stresses in the shell and how do they develop over time?
3. Can we attribute the reported crystallographic reorientation of some seashells to the internal stresses developed during incompatible growth?

1.4 Thesis Outline

The subsequent parts of the thesis are organized as follows: Chapter 2 introduces our kinematic framework with which we model the growth of a seashell; Chapter 3 provides the analytical and numerical solution method that is used to solve the resulting boundary-value problem; Chapter 4 presents the results from solving this problem with various kinematic inputs and levels of incompatibility, and draws conclusions about how these resulting internal stresses are linked to the observed structural changes in seashells. Finally, Chapter 5 gives a summary of the thesis and outlines future work to be done on the project.

Chapter 2

Theory

In this chapter, we develop a theoretical model for the growth of shell surfaces. Firstly, we introduce the problem setting and provide an overview of the kinematics involved in this growth process. To prepare the model for future integration with a thermodynamically consistent kinetic law, we utilize an arbitrary kinematic input. Additionally, we define and then minimize the elastic energy for the entire shell. Finally, we employ variational calculus to transform the energy minimization into a boundary-value problem, which we solve to determine the shape of the shell.

2.1 Kinematics

To answer the questions outlined in the problem statement (Section 1.3), we make some simplifying kinematic assumptions. For simplicity, the surface growth of the seashell is modeled in 3-D as the addition of infinitesimal rings around a solid core. Consider a single infinitesimal ring, mapped by the cylindrical coordinate system (τ, θ, Z) as seen in Figure 2-1. The ring has a nominal stress-free radius of R_j and a radial thickness of $d\tau$. The "time" of attachment τ is a pseudotime, due to the fact that it serves as a spatial coordinate within an individual ring, as well as a way to sequence the order of the addition of rings throughout the evolution of the shell. We make the assumption that the shell has a constant positive rate of addition of material ($d\tau$). Therefore, the pseudotime τ is a monotonically increasing variable.

From here on, we refer to τ as both time and a length coordinate.

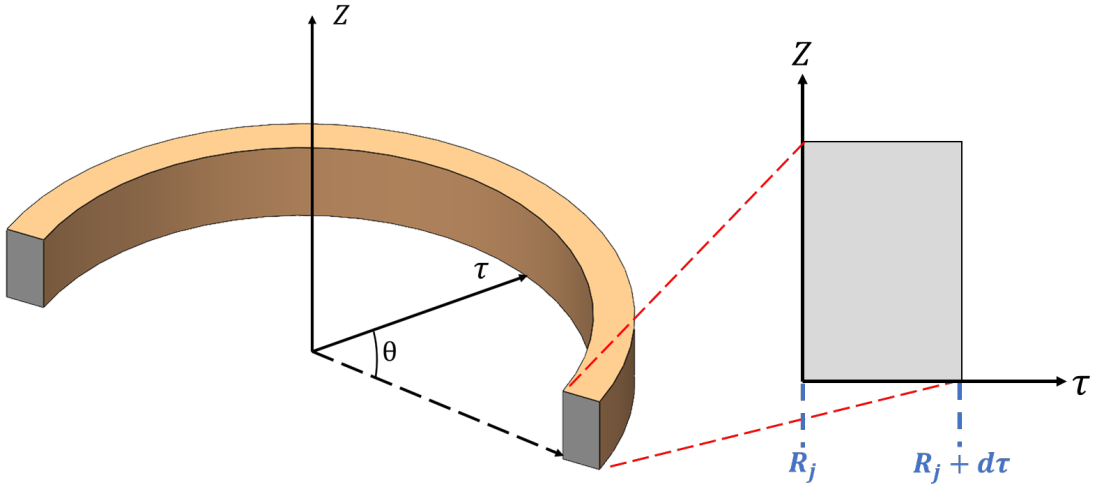

Figure 2-1: Axisymmetry of a single ring of the seashell and the associated cylindrical coordinate system.

As the shell grows, another infinitesimal ring of stress-free radius R_k is added. The change in stress-free radius between the rings, dR, is thus defined by

$$dR = R_k - R_j. \tag{2.1}$$

We hereby define the function $R(\tau)$ to be equal to the stress-free radius of each infinitesimal ring that was added to the shell at a give time τ. There are two possible types of surface growth in the system. The first type, compatible surface growth, adds no residual stress to the system while the second type, incompatible surface growth does impart stress to the shell. Let us first examine compatible surface growth. For the two rings to be compatible, the stress-free radius of the ring to be added R_k must be equal to the outer radius of the existing ring, $R_j + d\tau$. The time derivative of the radius function $R(\tau)$ is thus

$$R' = \frac{dR}{d\tau} = \frac{R_k - R_j}{(R_j + d\tau) - R_j} = \frac{d\tau}{d\tau} = 1$$

with the superposed prime hereby denoting differentiation with pseudotime $(.)' = d(.)/d\tau$. We now examine the case of incompatible growth. Incompatible growth

occurs when the stress-free radius of the ring to be added (R_k) is not equal to the outer radius of the existing ring $R_j + d\tau$.

$$R' = \frac{dR}{d\tau} = \frac{R_k - R_j}{(R_j + d\tau) - R_j} = \frac{R_k - R_j}{d\tau} \neq 1$$

This incompatibility between rings imparts residual stress to the system. As discussed in Section 1.3, the goal of this project is to solve the forward problem for an arbitrary kinematic input. The kinematic input is through the function $R(\tau)$ and controls the level of incompatibility introduced to the system. The system is solved with different $R(\tau)$ functions to test the following growth types:

- $R' = 1$, compatible growth, no stress added to the system
- $R' < 1$, incompatible growth, *compressive* stress added to the system
- $R' > 1$, incompatible growth, *tensile* stress added to the system

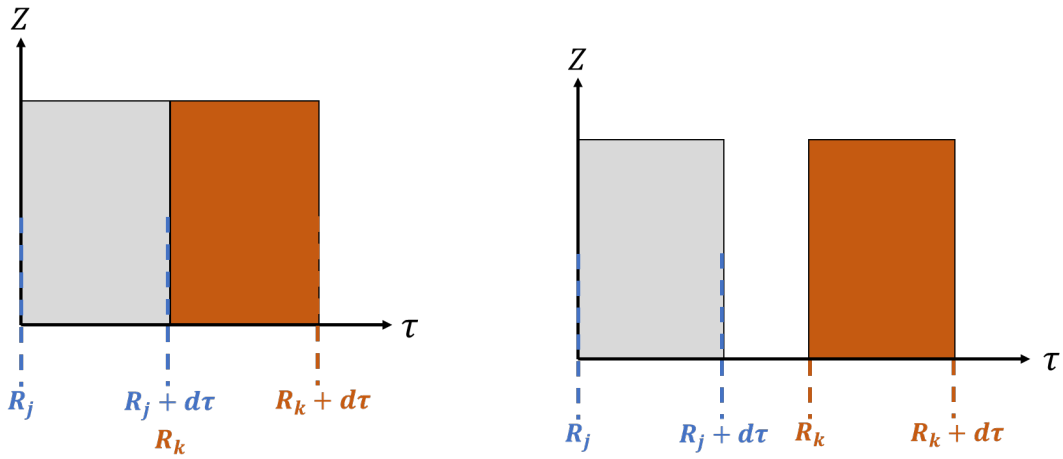

(a) Compatible ($R' = 1$) (b) Incompatible ($R' > 1$)

Figure 2-2: Mapping for the attachment of two arbitrary rings in the seashell

Let us now return to considering a single ring of the shell as our body. In the undeformed state, this ring occupies the region $R_i \leq \tau \leq R_i + d\tau$, $0 \leq \theta \leq 2\pi$, and $0 \leq Z \leq H$. The axisymmetric deformation field of the shell as a function of the

pseudotime τ and a function of height Z is written as:

$$r = \tau + \phi(\tau, Z) \qquad \theta = \Theta \qquad z = Z + \zeta(\tau, Z) \tag{2.2}$$

along the (τ, θ, Z) directions, respectively (Fig. 1(a)). τ is able to be used as the radial coordinate within an individual ring due to the fact that each ring is compatible on its own.

As we are using a cylindrical coordinate scheme, the deformation gradient that maps a ring of the shell from its deformed configuration (τ, Θ, Z) to its deformed configuration (r, θ, z) is $\mathbf{F}$:

$$\mathbf{F} = \begin{bmatrix} 1 + \frac{\partial \phi}{\partial \tau} & 0 & \frac{\partial \phi}{\partial Z} \\ 0 & 1 + \frac{\phi}{\tau} & 0 \\ \frac{\partial \phi}{\partial Z} & 0 & 1 + \frac{\partial \zeta}{\partial Z} \end{bmatrix} \tag{2.3}$$

Now that the deformation for a single ring is outlined, we consider how we map the deformation of the entire shell for the case of incompatible growth. As is shown in Figure 2-3, for the incompatible growth case, there is not a continuous mapping of the coordinate τ across the rings. In the reference configuration Ω_0, each axisymmetric ring has a volume of $V_1 = 2\pi R(\tau) d\tau H$. Let us imagine an imaginary compatible configuration in which each ring in the shell has the same mass as the original configuration, but the radial thickness of each ring has been changed from its original thickness, $d\tau$, to dR to assure that the end of one ring is at the same position of the beginning of the next ring. Changing the thickness of these incompatible rings changes the volume of each ring, and thus each ring undergoes a density change $\Delta\rho$ as it is mapped into an intermediate (imaginary) configuration Ω_i

$$\Delta\rho = \frac{\rho_2}{\rho_1} = m\frac{V_2}{V_1} = \frac{2\pi R(\tau) dR H}{2\pi R(\tau) d\tau H} = \frac{dR}{d\tau} = R'. \tag{2.4}$$

This density change is organized into a tensor that maps the change in radial thickness of a given ring from configuration Ω_0 to Ω_i. We refer to this tensor as the compatibility

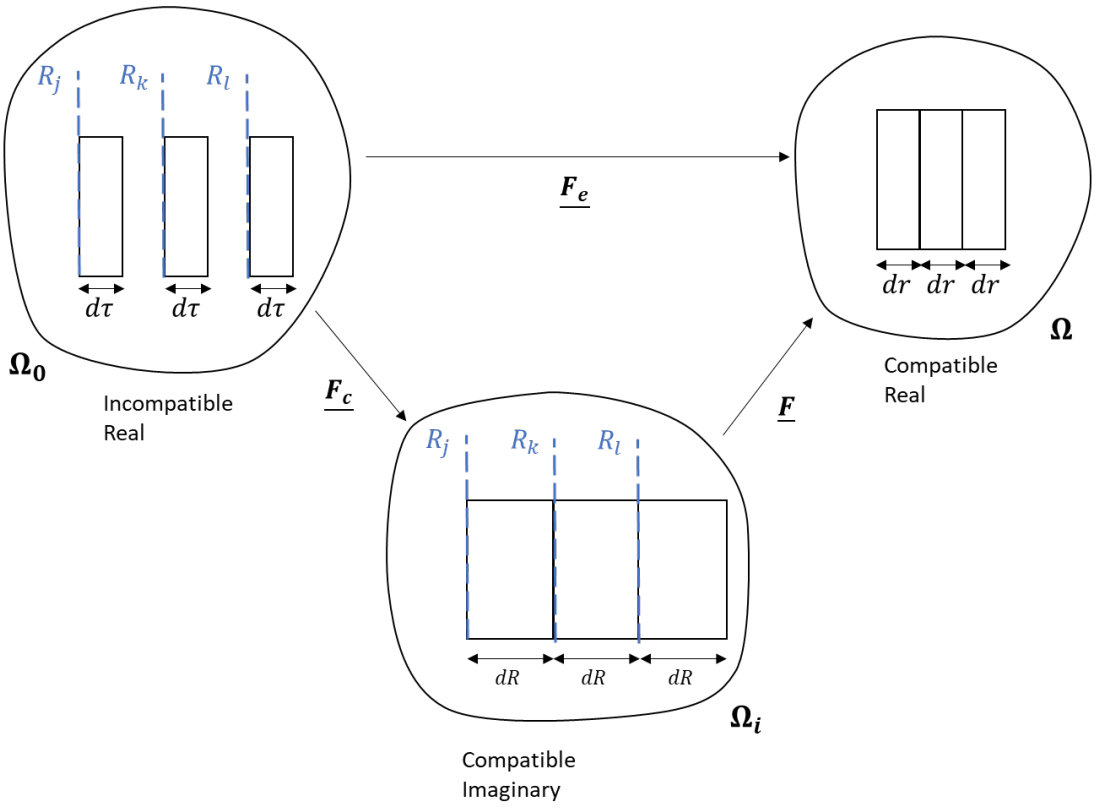

Figure 2-3: Kinematics of surface growth. Multiplicative decomposition of the deformation gradient $\mathbf{F_e}$ into compatibility $\mathbf{F_c}$ and deformation $\mathbf{F}$ parts.

tensor $\mathbf{F_c}$.

$$\mathbf{F_c} = \begin{bmatrix} R' & 0 & 0 \\ 0 & 1 & 0 \\ 0 & 0 & 1 \end{bmatrix} \tag{2.5}$$

This density change now allows the function $R(\tau)$ to be equal to τ within a single ring, enabling the substitution of the coordinate R for the coordinate τ in (2.3). The deformation gradient mapping a single ring from the initial configuration Ω_0 to its deformed configuration Ω now becomes

$$\mathbf{F_e} = \mathbf{F}\mathbf{F_c} = \begin{bmatrix} R'\left(1+\frac{\partial\phi}{\partial\tau}\right) & 0 & \frac{\partial\phi}{\partial Z} \\ 0 & 1+\frac{\phi}{R} & 0 \\ \frac{\partial\phi}{\partial Z} & 0 & 1+\frac{\partial\zeta}{\partial Z} \end{bmatrix} \tag{2.6}$$

Let us note that although we have used multiplicative decomposition to model our

growth, this decomposition is distinctly different from that of the typical growth study shown in Figure 1-4 and described in Section 1.2.2. In the typical growth study, the reference configuration is a compatible one, with the body able to be mapped continuously. The growth of the body requires the use of an imaginary incompatible configuration, and then requires elastic force to resolve this into a compatible deformed configuration. In our framework, the parts of the body, i.e. the rings, could be incompatible with each other in the real reference configuration. This necessitates the use of an imaginary configuration to attach these rings to one another (created through the density change of each ring), and the creation of mechanical forces when this configuration is relaxed into the deformed configuration.

We apply two internal constraints to the deformation field of a ring. The first constraint is incompressibility, which restricts the true deformation of the ring to only motion that preserves its volume. This constraint is enforced by requiring the determinant of the deformation gradient ($\mathbf{F_e}$), which maps the transition from the reference configuration Ω_0 to the deformed configuration Ω, is equal to 1

$$\det(\mathbf{F_e}) = R'\left(1+\phi'\right)\left(1+\frac{\phi}{R}\right)\left(1+\frac{\partial\zeta}{\partial Z}\right) = 1. \tag{2.7}$$

Considering only the first-order contributions, the incompressibility constraint (2.7) becomes

$$\phi' + \frac{\phi}{R} + \frac{\partial\zeta}{\partial Z} = \frac{1}{R'} - 1. \tag{2.8}$$

The second internal constraint is inspired by the Timoshenko–Ehrenfest beam theory [43], but is modified to apply to an axisymmetric body. We assume that within the shell, planes that are initially perpendicular to the radial axis remains planar even after deformation. Therefore, the radial deformation across the entire shell thickness is determined by analyzing only the top and bottom surfaces. This is achieved by observing that corresponding points on each surface in the reference configuration remain connected by a linear curve [10]. The equation for the radial

deformation of a ring through its thickness is thus

$$\phi(\tau, Z) = \phi_0(\tau) + (\phi_H(\tau) - \phi_0(\tau)) \frac{Z}{H}, \tag{2.9}$$

where $\phi_0(\tau) = \phi(\tau, 0)$ and $\phi_H(\tau) = \phi(\tau, H)$ represent the radial displacement of the top and bottom surfaces of an individual ring, respectively.

The Timoshenko–Ehrenfest beam theory does not provide equivalent kinematic assumptions for the normal displacement $\zeta(\tau, Z)$ in (2.2). However, combining the incompressibility constraint (2.8) and the Timoshenko–Ehrenfest hypothesis (2.9), then integrating the result over the thickness of the ring yields a quadratic relation in Z for the normal displacement ζ,

$$\zeta(\tau, Z) = \zeta_0(\tau) - \left(1 - \frac{1}{R'} + \phi_0' + \frac{\phi_0}{R}\right) Z - \left(\phi_H' - \phi_0' + \frac{\phi_H - \phi_0}{R}\right) \frac{Z^2}{2H}, \tag{2.10}$$

where ζ_0 emerges as an integration constant and represents the deformation at $Z = 0$, i.e. $\zeta_0 = \zeta(\tau, 0)$. For further reference, we write the vertical displacement of the top surface of the ring $\zeta_H = \zeta(\tau, H)$ as

$$\zeta_H = \zeta_0 - \left(1 - \frac{1}{R'} + \phi_0' + \frac{\phi_0}{R}\right) H - \left(\phi_H' - \phi_0' + \frac{\phi_H - \phi_0}{R}\right) \frac{H}{2}. \tag{2.11}$$

We use two kinematic constraints, namely incompressibility and the Timoshenko–Ehrenfest beam theory to reduce the functional set of possible deformation fields. It is now fully defined by a set of three unknown functions $(\phi_0, \phi_H, \zeta_0)$ that depend on the radial coordinate τ.

We also make the assumption that we are undergoing deformation in the linear range. The nonzero strain components for a single ring of the shell are represented

by

$$\begin{aligned}
\epsilon_{rr} &= R'\left(1+\phi_0'+\left(\phi_H'-\phi_0'\right)\frac{Z}{H}\right)-1 \\
\epsilon_{\theta\theta} &= \frac{\phi_0}{R}+\left(\phi_H-\phi_0\right)\frac{Z}{HR} \\
\epsilon_{zz} &= -\left(1-\frac{1}{R'}+\phi_0'+\frac{\phi_0}{R}\right)-\left(\phi_H'-\phi_0'+\frac{\phi_H-\phi_0}{R}\right)\frac{Z}{H} \\
\epsilon_{zr} &= \frac{1}{2}\left[\frac{\phi_H'-\phi_0'}{H}+\zeta_0'-\left(\phi_0''+\frac{\phi_0}{R}-\frac{\phi_0}{R^2}\right)Z-\left(\phi_H''-\phi_0''+\frac{\phi_H'-\phi_0'}{R}-\frac{\phi_H+\phi_0}{R^2}\right)\frac{Z^2}{2H}\right].
\end{aligned} \tag{2.12}$$

2.2 Energy Minimization

2.2.1 Elastic Energy

Single Ring

With the kinematics of the shell fully described, we proceed to finding its elastic energy. The shell is approximated as a linear neo-Hookean material. The constitutive relation for the strain energy density for the shell Ψ is thus

$$\Psi = \frac{E}{6}\left(I_1-3\right) \tag{2.13}$$

To find the value of I_1, the left-Cauchy Green tensor is calculated by multiplying the deformation gradient with its transpose

$$[\mathbf{B}] = [\mathbf{F}][\mathbf{F^T}] = \begin{bmatrix} \left(1+\phi'\right)^2+\frac{\partial\phi}{\partial Z}^2 & 0 & \frac{\partial\zeta}{\partial\tau}\left(1+\phi'\right)+\frac{\partial\phi}{\partial Z}\left(1+\frac{\partial\zeta}{\partial Z}\right) \\ 0 & \left(1+\frac{\phi}{R}\right)^2 & 0 \\ \frac{\partial\zeta}{\partial\tau}\left(1+\phi'\right)+\frac{\partial\phi}{\partial Z}\left(1+\frac{\partial\zeta}{\partial Z}\right) & 0 & \left(1+\frac{\partial\zeta}{\partial Z}\right)^2+\frac{\partial\zeta}{\partial\tau}^2 \end{bmatrix}. \tag{2.14}$$

I_1 is defined as the first invariant of the left-Cauchy Green tensor and is calculated as trace($\mathbf{B}$). The equation for I_1 is

$$I_1 = 3+2\left(\phi'+\frac{\phi}{R}+\frac{\partial\zeta}{\partial Z}\right)+\left(\phi'^2+\frac{\phi}{R}^2+\frac{\partial\zeta}{\partial Z}^2+\frac{\partial\phi}{\partial Z}^2+\frac{\partial\zeta}{\partial\tau}^2\right). \tag{2.15}$$

As outlined in Section 2.1, we assume that each ring in the shell is undergoing deformations that fall within the linear range. For this reason, we keep only quadratic terms in the elastic energy density; both the constant and linear terms are dropped. After substituting the first invariant (2.15) into the neo-Hookean constitutive relation, the strain energy density becomes

$$\Psi = \frac{E}{6}\left(\phi'^2 + \frac{\phi}{R}^2 + \frac{\partial\zeta}{\partial Z}^2 + \frac{\partial\phi}{\partial Z}^2 + \zeta'^2\right). \tag{2.16}$$

With the elastic energy density defined for a single ring as Ψ, the elastic energy for a single ring of the shell ΔU is found by integrating this energy density across the volume of a ring

$$\Delta U_j = \int_{R_j}^{R_j+\Delta\tau}\int_0^H\int_0^{2\pi} \Psi(\tau, Z) R\, d\theta\, dZ\, d\tau = 2\pi\Delta\tau \int_0^H \Psi(R_j, Z) R_j\, dZ\,. \tag{2.17}$$

Since the dependence of Ψ on Z is known, integration is performed directly to write

$$\Delta U_j = 2\pi\Delta R_j \tau \hat{f}(R_j). \tag{2.18}$$

where $\hat{f}(R) = f(\phi_0, \phi_H, \zeta_0, \phi_0', \phi_H', \zeta_0', \phi_0'', \phi_H'', \tau)$.

Entire Shell

After integrating the elastic energy density over the volume of a single ring, the total elastic energy U is obtained as the sum of energy in all rings. Considering rings of infinitesimal radial thickness, such that $\Delta\tau \to d\tau$, and thus $\Delta U \to dU$ we calculate the total energy of the shell from the integration

$$U = \int_0^{\tau_{max}} dU = 2\pi \int_0^{\tau_{max}} f(\phi_0, \phi_H, \zeta_0, \phi_0', \phi_H', \zeta_0', \phi_0'', \phi_H'', \tau) d\tau. \tag{2.19}$$

The inner and outer boundaries of the shell in the radial direction are defined as $\tau = 0$ and $\tau = \tau_{max}$ respectively.

2.2.2 Euler-Lagrange Equations

We now seek to minimize the elastic energy of the shell to find its equilibrium deformation field. This minimization is performed with the use of variational calculus. The Euler-Lagrange equations are used to convert the integrand of the elastic energy function into a boundary-value problem that we solve to find the geometry of the shell (the shape that produces the minimum elastic energy) at any given time. As seen in (2.19), the elastic energy is a second-order function of three unknowns (ϕ_0, ϕ_H, and ζ_0) and their derivatives, all of which depend on the pseudotime τ. For the second order energy function, the Euler-Lagrange equations are of the form

$$\frac{\partial f}{\partial q_i} - \frac{d}{d\tau}\frac{\partial f}{\partial q_i'} + \frac{d^2}{d^2\tau}\frac{\partial f}{\partial q_i''} = 0 \qquad i = 1, 2, 3 \tag{2.20}$$

with the substitution $q_i = \{\phi_0, \phi_H, \zeta_0\}$ used for compactness. The Euler-Lagrange equations output three equations, two fourth-order and one third-order, dependent on three unknowns (ϕ_0, ϕ_H, and ζ_0) and their derivatives. These equations make up a system of differential equations which we organize into matrix form.

$$\begin{bmatrix} A_1(\tau) & B_1(\tau) & \dots & M_1(\tau) & N_1(\tau) \\ A_2(\tau) & B_2(\tau) & \dots & M_2(\tau) & N_2(\tau) \\ A_3(\tau) & B_3(\tau) & \dots & M_3(\tau) & N_3(\tau) \end{bmatrix} \begin{bmatrix} \phi_0 \\ \phi_H \\ \zeta_0 \\ \phi_0' \\ \vdots \\ \zeta_0''' \\ \phi_0'''' \\ \phi_H'''' \end{bmatrix} + \begin{bmatrix} Z_1(\tau) \\ Z_2(\tau) \\ Z_3(\tau) \end{bmatrix} = \mathbf{0}. \tag{2.21}$$

The values of each of the variable coefficients $(A_i(\tau), B_i(\tau), ..., Z_i(\tau))$ are shown in Appendix A.

2.2.3 Boundary Conditions

The use of the Euler-Lagrange equations also produces two natural boundary conditions per unknown. These natural boundary conditions are of the form

$$\frac{\partial f}{\partial q_i'} - \frac{d}{d\tau}\frac{\partial f}{\partial q_i''} = 0 \qquad \frac{\partial f}{\partial q_i''} = 0 \qquad i = 1, 2, 3. \tag{2.22}$$

Five natural boundary conditions are produced corresponding to the three unknowns of the energy function (the 6^{th} natural boundary condition is trivial)

$$\begin{aligned} &60 + 80\phi_0' + 40\phi_H' + \frac{H^2(16\phi_0' + 9\phi_H')(2 + R')}{R^2} - \frac{H^2(16\phi_0 + 9\phi_H)(1 + 2R')}{R^3} \\ &-\frac{60}{R'} + (\frac{20(2\phi_0 + \phi_H - H\zeta_0'))}{R} + 40H\zeta_0'' - 16H^2\phi_0''' - 9H^2\phi_H''' = 0 \end{aligned} \tag{2.23}$$

$$-16H\phi_0 - 9H\phi_H + R(16H\phi_0' + 9H\phi_H' + R(-40\zeta_0' + 16H\phi_0'' + 9H\phi_H'')) = 0 \tag{2.24}$$

$$\begin{aligned} &60 + 40\phi_0' + 80\phi_H' + \frac{3H^2(3\phi_0' + 2\phi_H')(2 + R')}{R^2} - \frac{3H^2(3\phi_0 + 2\phi_H)(1 + 2R')}{R^3} \\ &-\frac{60}{R'} + (\frac{20(\phi_0 + 2\phi_H - H\zeta_0'))}{R} + 20H\zeta_0'' - 9H^2\phi_0''' - 6H^2\phi_H''' = 0 \end{aligned} \tag{2.25}$$

$$-9H\phi_0 - 6H\phi_H + R(9H\phi_0' + 6H\phi_H' + R(-20\zeta_0' + 9H\phi_0'' + 6H\phi_H')) = 0 \tag{2.26}$$

$$2H\phi_0 + H\phi_H - R(2H\phi_0' + H\phi_H' + R(-6\zeta_0' + 2H\phi_0'' + H\phi_H'')) = 0. \tag{2.27}$$

As we have a system of equations (2.21) with 11 unknowns, we need to apply 11 boundary conditions. To enforce axisymmetry, we apply a set of geometric boundary conditions at the innermost edge such that

$$\tau = 0: \qquad \phi_0 = 0, \quad \phi_H = 0, \quad \zeta_0 = 0, \quad \zeta_H' = 0, \quad \zeta_0' = 0. \tag{2.28}$$

This ensures that the first ring added to the shell is stress-free and compatible ($r = R_i$), and constrains the vertical motion of the entire shell. To complete the description of the problem we use the natural boundary conditions. At $\tau = 0$ we employ (2.26), and at the free edge ($\tau = \tau_{max}$) we apply (2.23)-(2.27).

Chapter 3

Solution Method

In Chapter 2, we discussed the kinematics of the shell and utilized the Euler-Lagrange equations to minimize the elastic energy throughout the shell. This process transformed the function representing the total elastic energy into a boundary-value problem (BVP) along with its associated boundary conditions. In the following chapter, we present our approach to solve this BVP.

3.1 System Characterization

The system of differential equations resulting from our use of the Euler-Lagrange equations (2.21) has three important characteristics. Firstly, as a result of our assumption of linear elasticity, all of the differential equations in this system are linear, with each equation having a linear dependence on the three dependent variables and their derivatives. The second characteristic of note is that the system of differential equations is nonhomogenous, as there are constant terms that do not depend on any of the unknowns or their derivatives. The final characteristic of this system of differential equations is that the coefficients of the dependent variables and their derivatives are all nonconstant.

3.2 Reduction of Order

These unique characteristics combined with the high-order of the equations make it difficult to solve the system in its original form. We thus represent the system in a different form that allows a simpler solution method.

$$\begin{bmatrix} L_1(\tau) & M_1(\tau) & N_1(\tau) \\ L_2(\tau) & M_2(\tau) & N_2(\tau) \\ L_3(\tau) & M_3(\tau) & N_3(\tau) \end{bmatrix} \begin{bmatrix} \zeta_0''' \\ \phi_0'''' \\ \phi_H'''' \end{bmatrix} = - \begin{bmatrix} A_1(\tau) & \dots & K_1(\tau \\ A_2(\tau) & \dots & K_2(\tau) \\ A_3(\tau) & \dots & K_3(\tau) \end{bmatrix} \begin{bmatrix} \phi_0 \\ \phi_H \\ \zeta_0 \\ \vdots \\ \zeta_0'' \\ \phi_0''' \\ \phi_H''' \end{bmatrix} - \begin{bmatrix} Z_1(\tau) \\ Z_2(\tau) \\ Z_3(\tau) \end{bmatrix}. \quad (3.1)$$

Using substitution, the system of fourth-order and third-order equations can be reduced to a system of first-order equations. This substitution scheme, called *reduction of order*, works by substituting a new variable for each derivative of the dependent variables of the system - up to but not including the highest order derivative of that variable. This substitution is carried out through the introduction of first-order equations into the system. Each new equation introduces one new unknown into the system of equations. The full set of equations to be introduced to the shell system is shown below.

$$\begin{array}{lll} \underline{\phi_0} & \underline{\phi_H} & \underline{\zeta_0} \\ \phi_{01} = \phi_0' & \phi_{H1} = \phi_H' & \zeta_{01} = \zeta_0' \\ \phi_{02} = \phi_0'' & \phi_{H2} = \phi_H'' & \zeta_{02} = \zeta_0'' \\ \phi_{03} = \phi_0''' & \phi_{H3} = \phi_H''' & \end{array} \quad (3.2)$$

After the reduction of order, 8 equations are introduced into the system, and the system is now 11 first-order differential equations with 11 unknowns. It is represented

in the matrix form below.

$$\left[\begin{array}{c|ccc} \mathbf{I} & \multicolumn{3}{c}{\mathbf{0}} \\ \hline \mathbf{0} & L_1(\tau) & \dots & N_1(\tau) \\ & L_2(\tau) & \dots & N_2(\tau) \\ & L_3(\tau) & \dots & N_3(\tau) \end{array}\right] \begin{bmatrix} \phi_0 \\ \phi_H \\ \zeta_0 \\ \vdots \\ \zeta_0'' \\ \phi_0''' \\ \phi_H''' \end{bmatrix}' = - \left[\begin{array}{ccc|ccc} \multicolumn{3}{c|}{\mathbf{0}} & \multicolumn{3}{c}{\mathbf{I}} \\ \hline A_1(\tau) & \dots & & D_1(\tau) & \dots & K_1(\tau) \\ A_2(\tau) & \dots & & D_2(\tau) & \dots & K_2(\tau) \\ A_3(\tau) & \dots & & D_3(\tau) & \dots & K_3(\tau) \end{array}\right] \begin{bmatrix} \phi_0 \\ \phi_H \\ \zeta_0 \\ \vdots \\ \zeta_0'' \\ \phi_0''' \\ \phi_H''' \end{bmatrix} - \begin{bmatrix} Z_1(\tau) \\ Z_2(\tau) \\ Z_3(\tau) \end{bmatrix}$$

This system of equations can be more simply described in the form

$$[L(\tau)]\{y'\} = [S(\tau)]\{y\} + \{b(\tau)\}. \tag{3.3}$$

After multiplying (3.3) by $\mathbf{L}(\tau)^{-1}$ with the goal of isolating the vector of derivatives, the system of equations becomes

$$y' = \mathbf{M}(\tau) * y + \mathbf{B}(\tau) \tag{3.4}$$

with the matrix of variable coefficients $\mathbf{M}(\tau) = \mathbf{L}(\tau)^{-1}\mathbf{S}(\tau)$ and the matrix of variable constants $\mathbf{B}(\tau) = \mathbf{L}(\tau)^{-1}b(\tau)$.

3.3 Numerical Implementation

3.3.1 System Setup

Euler-Lagrange Equations

The first step in the numerical implementation of this problem is to generate the Euler-Lagrange Equations with which the displacement field that minimizes the energy of the shell is found. We leverage the Mathematica function `EulerEquations` to generate these equations. We write a Mathematica script that takes the equations

(2.9, 2.10) that describe the radial displacement ϕ and the axial displacement ζ as its input. It then computes the elastic energy density (2.16) from these displacement field equations, and integrates the elastic energy over the circumference and thickness to obtain the energy function in (2.19). The function `EulerEquations` then returns the three Euler-Langrange equations and the natural boundary conditions with which we define our system.

Reduction of Order

The second stage of the numerical implementation process carries out the reduction of order scheme to convert the output of the Euler-Lagrange equations (2.21) to the desired first order form of (3.4). We write a MATLAB script, `Reduction_of_Order.m`, to implement the scheme. The script takes in two inputs: the coefficient array $\mathbf{S}(\tau)$ and the constant vector $b(\tau)$. It performs the reduction of order by subtracting the coefficients from both sides of the equations to convert (2.21) to (3.1), and then padding out the coefficient array with the corresponding identity and zero matrices. After multiplying (3.3) by $\mathbf{L}(\tau)^{-1}$ with the goal of isolating the vector of derivatives, the system of equations reaches its final first order form (3.4).

3.3.2 Solving the Boundary-Value Problem

With the system of equations now reduced to being first-order, the final step in the computational framework is to solve the boundary-value problem. As discussed in Section 2.2.3, the problem is solved across the entire shell, with the interior boundary of the shell represented as $\tau = 0$ and the exterior boundary denoted by $\tau = \tau_{max}$. The problem is solved for the unknown vector $\vec{y}$ which is compromised of the three unknown functions (ϕ_0, ϕ_H, and ζ_0) and their derivatives. As discussed in Section 3.1, the shell is described by a system of equations that are nonhomogenous and have nonconstant coefficents. This system cannot be solved using direct analytical solution methods.

Instead, the boundary-value problem is integrated numerically. We utilize the

built-in MATLAB routine `bvp4c` to solve the integration problem (i.e. find the 11 unknowns) across the meshed time domain. The `bvp4c` function is able to solve both linear and nonlinear boundary-value problems. It relies on an iteration structure for solving systems of equations, using finite-difference code to implement the three-stage Lobatto IIIa formula. The `bvp4c` function thus provides a C^1 continuous solution that is fourth-order accurate across the problem's domain. Since it is an iteration scheme, the algorithm requires the user to input an initial guess for the solution [24].

The `bvp4c` function takes up to four input items. The first item, `bvpfcn`, is a function that constructs the system of equations to be solved at a given time step. This system is directly input from the `Reduction_of_Order.m` script, and is the right hand side of (3.4). The second input item is `bcfcn`, a function that constructs a matrix of boundary conditions to be applied at a given time step. For this input, we use a vector of the eleven boundary conditions found in (2.28). The third input item is `solinit`, which is a function that creates the initial guess to be used in the iteration structure. After extensive testing, we found that the output solution for the shell problem did not show dependence on this initial guess. For simplicity, a 11-row vector of ones is chosen as the initial solution guess at each time step. The final input item to `bvp4c` is the set `opts`. This structure allows modification of the accepted solution tolerance and statistics to be displayed.

Chapter 4

Results & Discussion

In this section, we present the results of the numerical solution of the boundary-value problem using the method outlined in Section 3. We begin by testing the solution method in the case of compatible growth. Next, we explore the effect of multiple parameters on the final solution. Then, we solve the seashell problem for different types of incompatible growth. For each growth scenario, we examine the shape of the shell and investigate the internal stresses that arise. Finally, we draw conclusions about the factors that are potential explanations for the real crystallographic reorientation observed in seashells.

4.1 Compatible Growth Validation

We first examine the compatible growth case to validate our solution method. An arbitrary kinematic input $R(\tau)$ must be selected to produce this growth case. As discussed in Section 2.1, the compatible growth case requires the derivative of the arbitrary kinematic input, $R'(\tau) = 1$. To find the corresponding kinematic input $R(\tau)$, we integrate the compatible growth constraint

$$R(\tau) = \int R'(\tau)\, d\tau = \int 1\, d\tau = \tau + C. \tag{4.1}$$

An initial value is then chosen to eliminate the resulting constant of integration. We hereby define the constant R_i, as $R(0) = R_i$. The kinetic input for the compatible growth case becomes

$$R(\tau) = \tau + R_i. \tag{4.2}$$

Because of the fact that R appears in the denominator throughout many equations in our kinematic model (2.6, 2.10, 2.16, etc.) a nonzero initial radius must be selected. A choice of 0 for the initial radius of the shell would lead to a singularity in the model's solution. For now, we choose $R_i = H$. The impact of this choice is investigated in Section 4.2. For our analysis in this section, we nondimensionalize our time coordinate τ by dividing by H, allowing us to track the shell growth by its aspect ratio a.

$$a = \frac{\tau}{H} \tag{4.3}$$

The maximum aspect ratio is thus denoted by a_{max}.

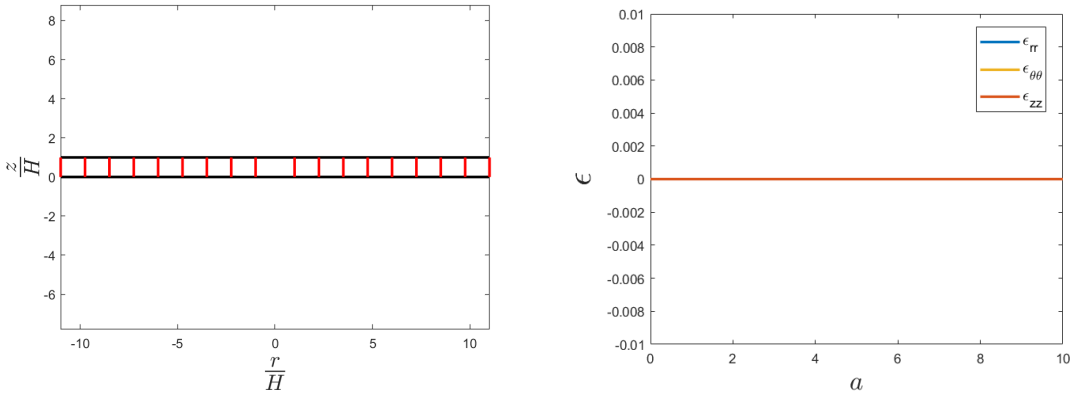

(a) Deformed Shell (b) Normal Strains

Figure 4-1: Compatible growth ($R_i = H$, $a_{max} = 10$).

The in-plane deformation field and the corresponding normal strains of the shell for compatible growth are shown in Figure 4-1. In the deformation plot, the lines shown in black represent the top and bottom surface of each ring in the deformed configuration. The vertical red lines are added to the shell to denote intervals of rings that have been added to the shell at a corresponding aspect ratio a_j. As expected, each ring added to the shell undergoes no deformation in the compatible growth case,

and no force is required to affix the ring to be added to the existing shell. Thus, the shell is able to grow in the radial direction without accumulating any stress, as there is no energy penalty for growth in this direction. The red lines in Figure 4-1a remain vertical throughout the radius of the shell, confirming that there is no bending moment experienced by the shell. The normal strains being zero verify the zero stress condition under linear elasticity.

4.2 Incompatible Growth

With the boundary-value problem solution method verified for the compatible growth case, we now proceed to using the model to investigate incompatible growth cases. As discussed in Section 2.1, the incompatible growth case requires the derivative of the arbitrary kinematic input, $R'(\tau) \neq 1$. We operate under the simplifying assumption that $R'(\tau)$ is a constant, A. We hereby refer to this constant as the linear incompatibility coefficient. To find the corresponding input $R(\tau)$, we integrate this value for the derivative in the same manner as the compatible growth case, using R_i as the initial value for the kinematic input.

$$R(\tau) = \int R'(\tau)\, d\tau = \int A\, d\tau = A\tau + R_i \tag{4.4}$$

The resulting kinetic input is a linear function of τ. We see from (4.4) that for the case $A = 1$ simplifies to the compatible growth case.

We first investigate the compressive linear incompatibility case. Per Section 2.1, this growth case occurs when $A < 1$. The deformation fields for $A = 0.5$ and $A = 0.1$ are shown in Figure 4-2. Unlike the compatible growth cases, the shell is deformed in the vertical direction (z). This deformation increases as the radial coordinate in the deformed configuration r increases. The red lines in each compressive case also have a finite slope, showing that each ring and the shell as a whole are experiencing bending. Due to the compressive forces in the radial direction, the vertical thickness of the innermost ring has increased from its initial height of H for both the $A = 0.5$ and $A = 0.1$ cases. Comparing these two cases, we see that as A decreases,

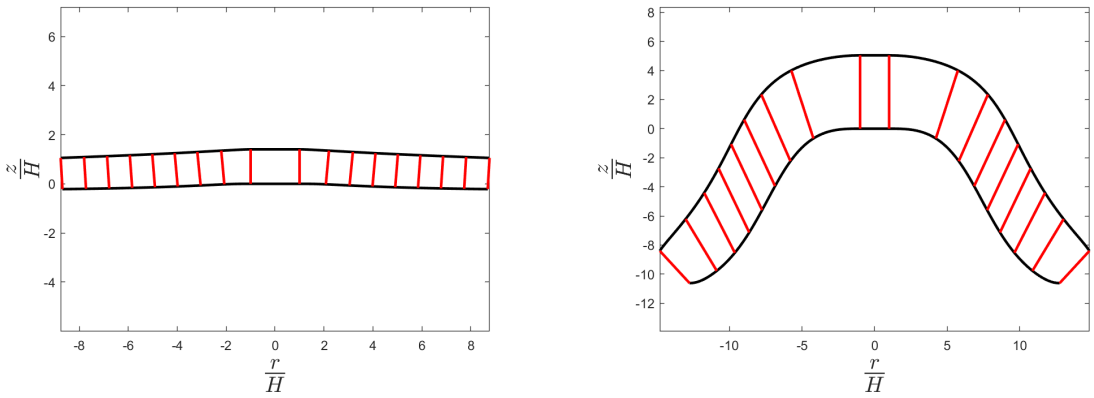

(a) $A = 0.5$ (b) $A = 0.1$

Figure 4-2: Compressive incompatible growth deformation fields ($A\tau + R_i$, $R_i = H$, $a_{max} = 10$).

the amount of compressive incompatibility, deformation, and bending all increase. Further discussion on the effect of A and the stress in the compressive case is left to Section 4.2.2.

We next investigate the tensile linear incompatibility case. Per Section 2.1, this growth case occurs when $A > 1$. The deformation field for the case of $A = 1.5$ and $A = 2$ is shown in Figure 4-3. The vertical deformation of the shell is rendered insignificant by the rapid expansion of the shell. Due to the tensile forces in the radial direction, the vertical thickness of the innermost ring decreases from its initial height of H. The shell effectively thins out as it stretches in the radial direction.

As a result of this initial comparison of the compressive and tensile growth cases, we decide to conduct the rest of our analysis using only compressive incompatibility. This growth case shows more interesting behavior, including greater vertical displacements of each ring and the bending of the shell, two behaviors that parallel the reported changes in microstructure of seashells in nature.

Impact of R_i

We now return to our choice of the initial radius of the shell, $R_i = H$. The selection of a small value for this parameter enables us to study the potential behaviors at early stages of growth, but the value must be large enough to avoid the introduction of a

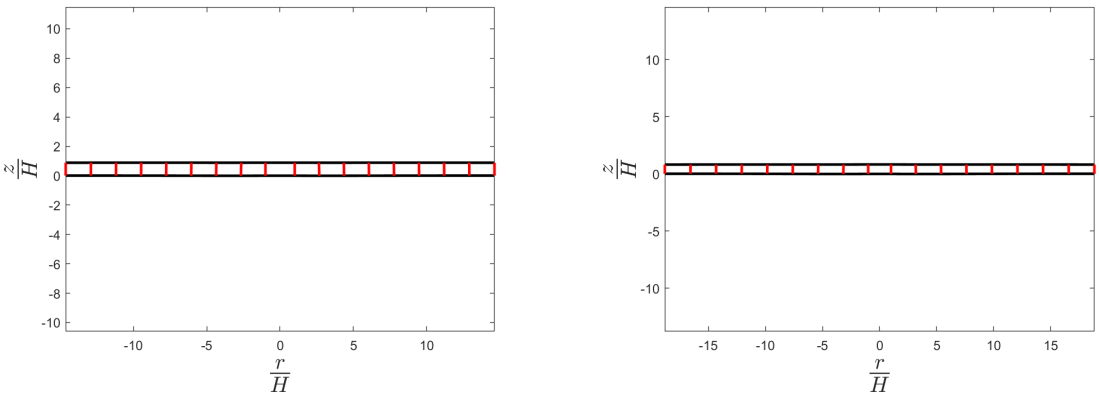

(a) $A = 1.5$ (b) $A = 2$

Figure 4-3: Tensile incompatible growth deformation fields ($A\tau + R_i$, $R_i = H$, $a_{max} = 10$).

singularity into the model. We use the compressive linear incompatibility growth case to examine the effect of R_i. Figure 4-4 shows how this initial radius value alters the solution for this growth case. Larger values of R_i help reduce the shape changing effect

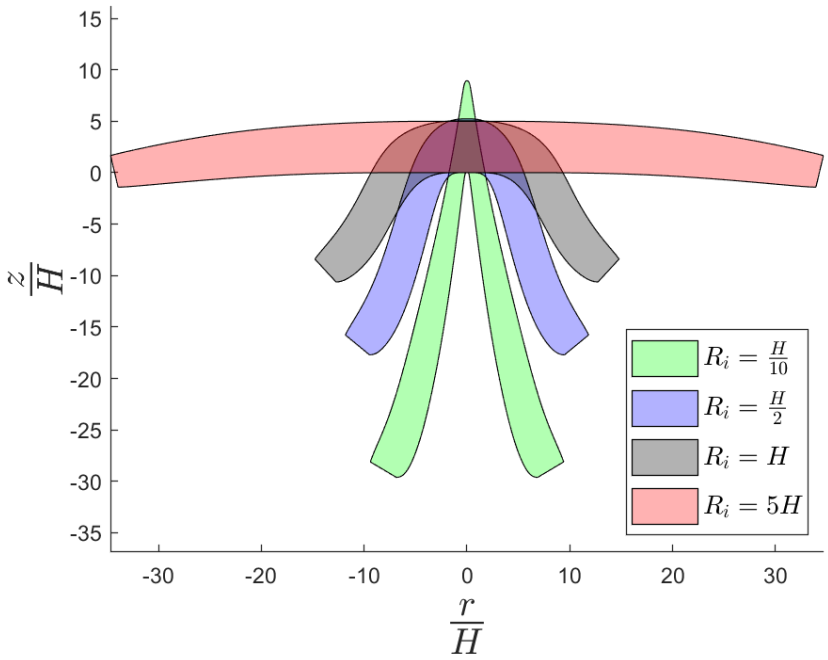

Figure 4-4: Effect of R_i on compressive linear incompatibility solution ($A\tau + R_i$, $A = 0.1$, $a_{max} = 10$)

of incompatibility. Conversely, as the initial radius moves towards 0, the influence

of the singularity becomes dominant as the shape of the deformed shell is collapsed. The choice of $R_i = H$ during the incompatible growth is reasonable, as this value is as large enough to avoid causing terms in the minimized energy to become singular, but small enough to allow us to study the early stages of growth. We continue using this value for R_i throughout the remainder of Section 4 to help investigate the effects of other input parameters on the solution.

Impact of A

With the selected value for R_i justified and the scope of the incompatible growth case narrowed to just examining kinematic inputs that produce compressive forces, we now investigate the effect of the linear incompatibility coefficient A. Figure 4-5 shows the deformed shell for various linear incompatible kinematic inputs. As expected, the larger the value of A, i.e. the closer the value is to 1, the more similar the shape of the shell is to the compatible growth case. The smaller the value of A, the more incompatibility is introduced to the system. This leads to increased vertical displacements, increased thickness of the shell, and more bending experienced by the shell. Our aim when choosing a value for A is to choose a value that produces

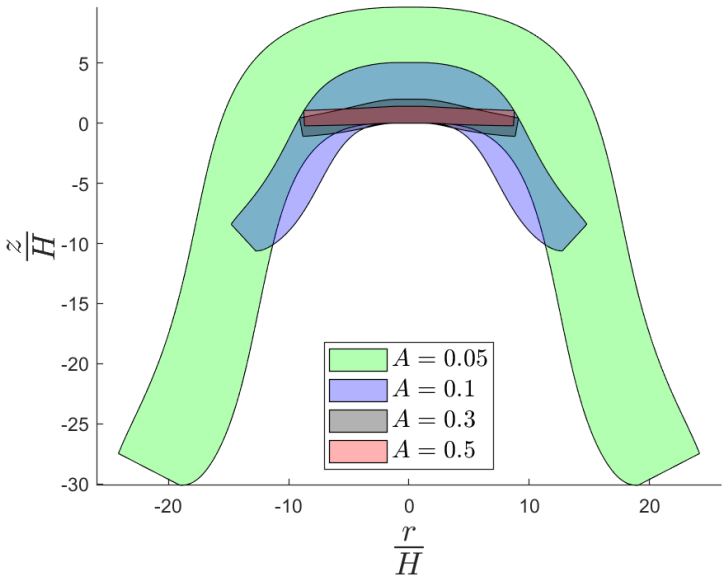

Figure 4-5: Effect of A on compressive linear incompatibility solution ($A\tau + R_i$, $R_i = H$, $a_{max} = 10$).

significant bending in the shell so that the sensitivity of the incompatible growth case can be fully studied, but does not produce a deformation so large that the assumptions of linear elasticity made in the definition of the kinematic framework are violated. Thus, $A = 0.1$ is selected for the linear incompatibility coefficient and used to study the growth process of the shell.

4.2.1 Growth Process

After setting the values for both A and R_i, we now examine the growth process (how the shell's shape evolves over time) for the case of compressive linear incompatibility. With the previous analysis being done at a fixed aspect ratio of $a_{max} = 10$, the maximum aspect ratio is now incrementally increased from a value of nearly 0 to a final value of 10. Figure 4-6 shows the deformation field of the shell at various sample points from this time period. The red lines in these plots denote the outermost edge (in the radial direction) of the rings added aspect ratios of 1.25 ($a = 1.25, 2.5, ..., 10$). As previously seen in Section 4.2, the shell initially starts out growing in the radial direction with minimal vertical displacement occurring. At some time prior to $a = 2.5$, the shell begins to grow in the vertical direction as well as the horizontal direction. This diagonal growth continues through the middle of the time range, until the shell reaches the deformation field at $a_{max} = 10$.

Now that we have a qualitative sense on how the shell evolves, we perform quantitative analysis on the reorientation of the shell and investigate the degree of bending in the early stages of the growth process. In Figure 4-6a, we see that bending has already started at a shell aspect ratio of $a_{max} = 2.5$. We thus focus our analysis on this section, refining our maximum aspect ratio to be between 0 and 2.5. The deformation field plots from this range is shown in Figure 4-7. The colored lines in these plots again represent the outermost edge of the rings added at aspect ratios of 0.3125 ($a = 0.3125, 0.625, ..., 0.25$). To measure the degree of bending of in a single ring throughout the early stages of growth process, we track the angle that the outermost edge of the ring makes with the horizontal line $\frac{z}{H} = 0$. A vertical edge with a 90° angle shows that a ring, while a more acute angle shows that the ring is experiencing

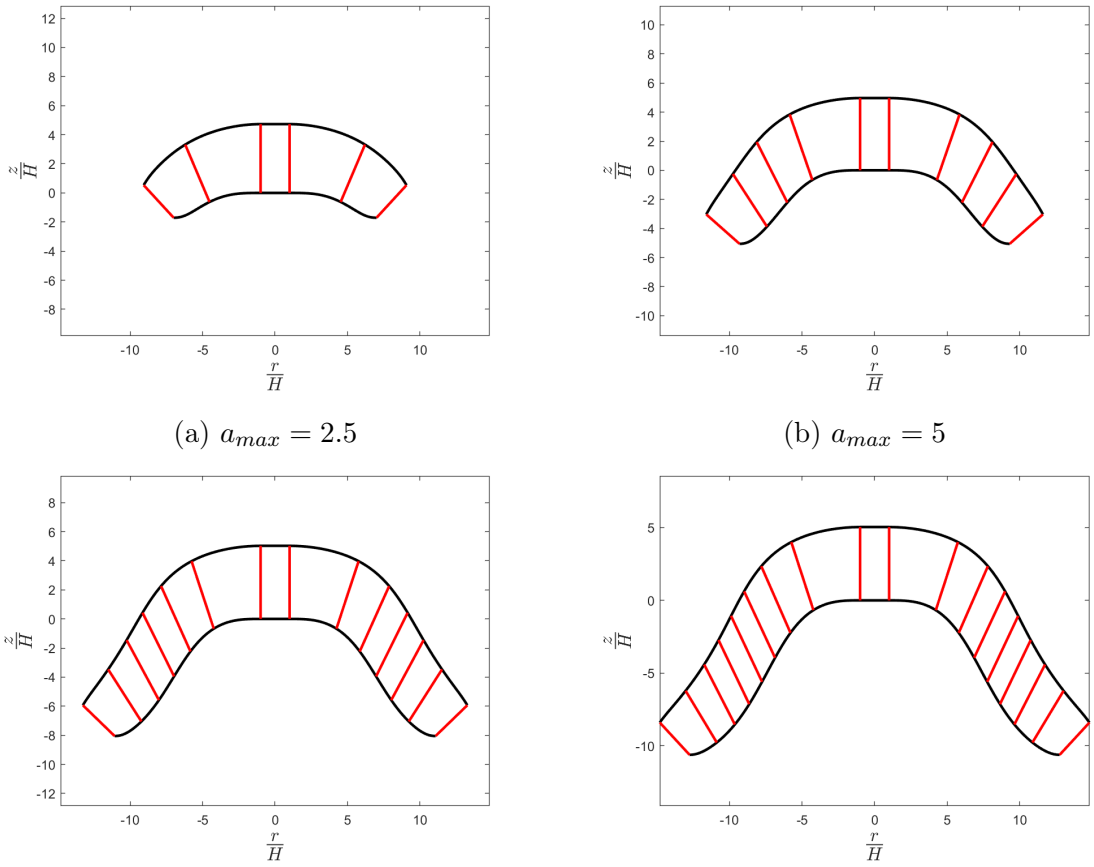

(a) $a_{max} = 2.5$

(b) $a_{max} = 5$

(c) $a_{max} = 7.5$

(d) $a_{max} = 10$

Figure 4-6: Linear incompatible growth process for sampled aspect ratios, ($A\tau + R_i$, $A = 0.1$, $R_i = H$)

bending. The ring edges corresponding to $a = 0.3125$ and $a = 0.9375$ are selected as samples to be used in the angle tracking analysis. These edges are shown in blue and magenta respectively in Figure 4-7. The angle of the sampled ring edges over time are shown in Figure 4-8.

At the aspect ratio of $a_{max} = 0.313$, the shell does not show significant vertical displacement, but the top edge of the shell is just starting to bend. At this point, the edge of the ring is nearly vertical at $\sim 88°$. After this point the top layer is vertically displaced and bending begins, followed by the bottom layer and the angle of the rings with the horizontal decreases. Interestingly, the angle of these sampled rings is non-monotonic. A ring edge has its maximum, or most vertical, angle upon being added to the shell. At an aspect ratio shortly after the ring's addition, the ring

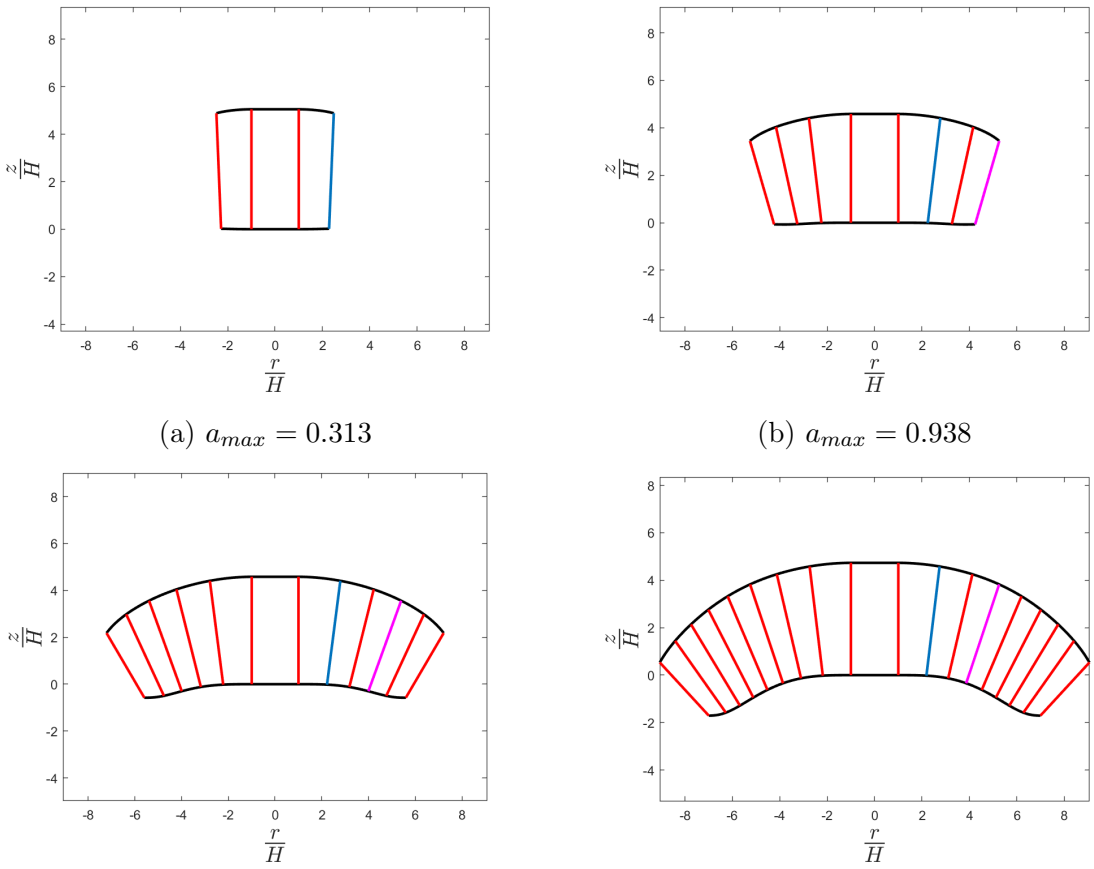

(a) $a_{max} = 0.313$

(b) $a_{max} = 0.938$

(c) $a_{max} = 1.56$

(d) $a_{max} = 2.5$

Figure 4-7: Early stages of linear incompatible growth growth process for sampled aspect ratios, ($A\tau + R_i$, $A = 0.1$, $R_i = H$).

reaches its minimum, most horizontal angle and thus its highest degree of bending. Similar to what was examined in the initial deformation field analysis, after a certain aspect ratio, $a = 0.6$, the continued growth of the shell does not impart any significant bending to the rings close to the center of the shell, with the angle of our sampled rings remaining constant.

4.2.2 Evolution of Stress

After conducting both qualitative and quantitative analysis on the shape of the shell and its associated deformation field, we now perform a stress analysis of the system in an effort to further understand our previous observations. Since we are in the linear elastic range, we can calculate the stress tensor at a given point in time from the

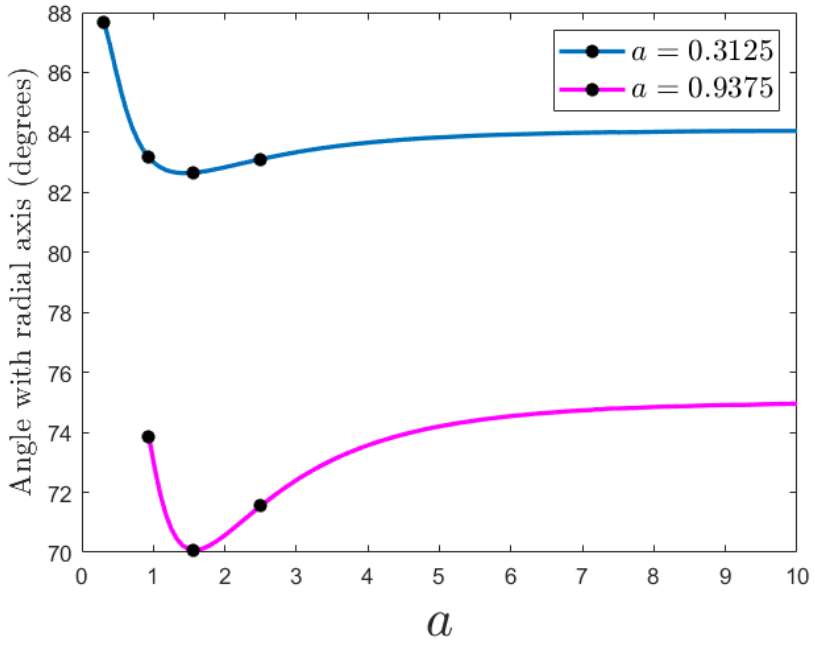

Figure 4-8: Angle with horizontal for radial edge of two sampled shell rings ($A\tau + R_i$, $A = 0.1$, $a_{max} = 10$).

strain tensor using $\boldsymbol{\sigma} = Y\boldsymbol{\epsilon}$. The equation for the strain components of the seashell are shown in (2.1).

As outlined in the problem statement for this thesis (Section 1.3), our goal is to calculate the internal stresses generated by a given incompatible growth case, and to track their development over time. For the purposes of this paper, we continue with the compressive linear incompatible growth case from the previous sections - $A\tau + R_i$ with $A = 0.1$, $R_i = H$. In the prior section, the qualitative analysis performed on the shell shape showed that bending begins in the earlier stages of the shell growth when the shell aspect ratio is less than 2.5. We thus maintain our focus on this section, keeping our maximum shell aspect ratio between 0 and 2.5. The normal stress components for sampled shell lengths in this range are shown in Figure 4-9.

Based on the plots in Figure 4-9, the value of the normal stress in the radial direction remains almost unchanged regardless of shell length, applying a constant compressive pressure to the shell as it grows in the radial direction. This is as expected given the compressive linear kinetic input we use for this analysis. At short shell

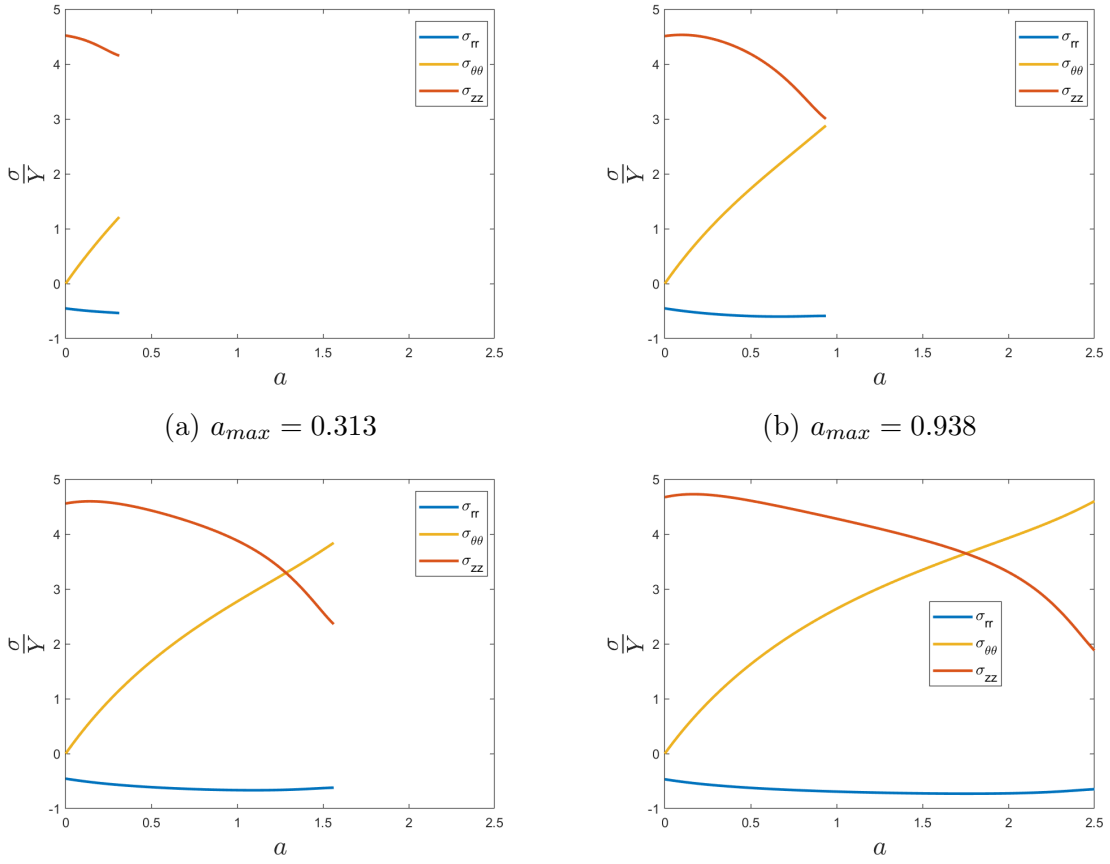

(a) $a_{max} = 0.313$ (b) $a_{max} = 0.938$

(c) $a_{max} = 1.56$ (d) $a_{max} = 2.5$

Figure 4-9: Internal normal stresses created due to the incompatible growth of the shell for samped aspect ratios ($A\tau + R_i$, $A = 0.1$, $R_i = 0.1$).

lengths, the normal stress in the vertical direction σ_{zz} imparts a large tensile stress to the shell. Over time, the shell displays some stress relaxation, decreasing this stress in the vertical direction across the length of the layer. This stress relaxation corresponds to a sharp increase in the circumferential stress, $\sigma_{\theta\theta}$, over the length of the shell.

The value of σ_{zz} over time is of particular interest to us in this analysis as this stress acts in the same (vertical) direction that the shell is deforming into for the incompatible growth case, as seen in Figure 4-7. Figure 4-10 provides a plot of σ_{zz} for the sampled shell aspect ratios on the same set of axes. When the plots of the deformation field are examined alongside this plot of the vertical stress, some powerful conclusions can be drawn. Regardless of shell length, rings near the center of the shell $\tau = 0$ experience a large tensile stress in the vertical direction. This stress

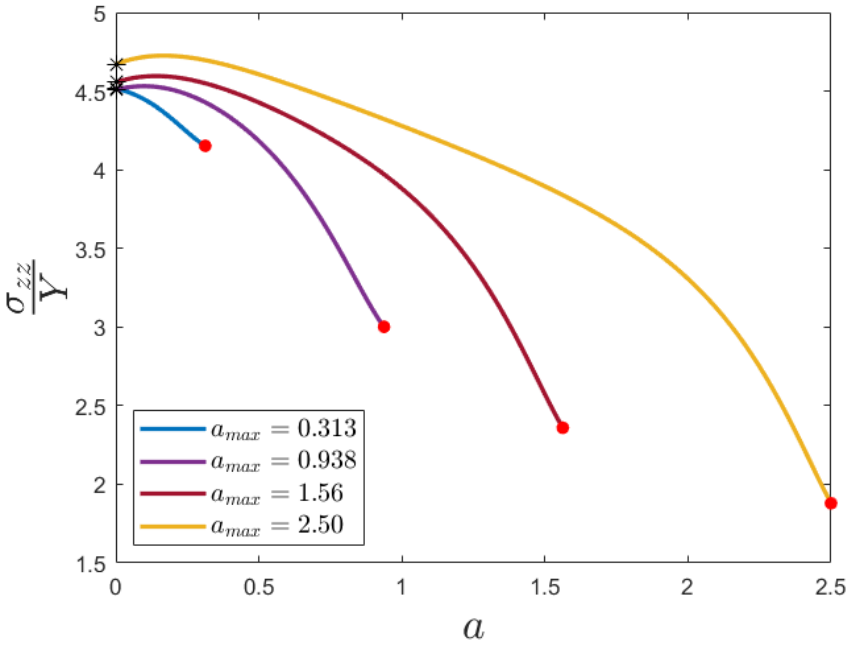

Figure 4-10: Stress in the vertical direction over the length of the shell in the early stages of the growth.

of the inner rings corresponds with their lack of vertical displacement. Meanwhile, the exterior of the shell experiences less and less stress as the shell length increases, which corresponds with the increasing vertical displacement of the shell exterior over time. Thus, there is a significant inverse correlation between the magnitude of the vertical displacement ζ and the value of σ_{zz}. Initially, the shell is experiencing a large amount of internal stress in the vertical direction due to the incompatible growth. As a result, it seeks to relax this internal tensile stress by bending and beginning to grow in the vertical direction. The growth in this direction sufficiently relaxes this internal stress.

Examining how the values of σ_{zz} at for the center of the shell ($a = 0$) and its exterior ($a = a_{max}$) change over time provides additional insight (Figure 4-11). When the shell is sufficiently short, the normal stress in the vertical direction is constant throughout the length of the shell and the shell is not experiencing any bending. At some aspect ratio during the early stages of development, the need to relax this vertical tensile stress causes the shell to bend and it grows in both the radial and

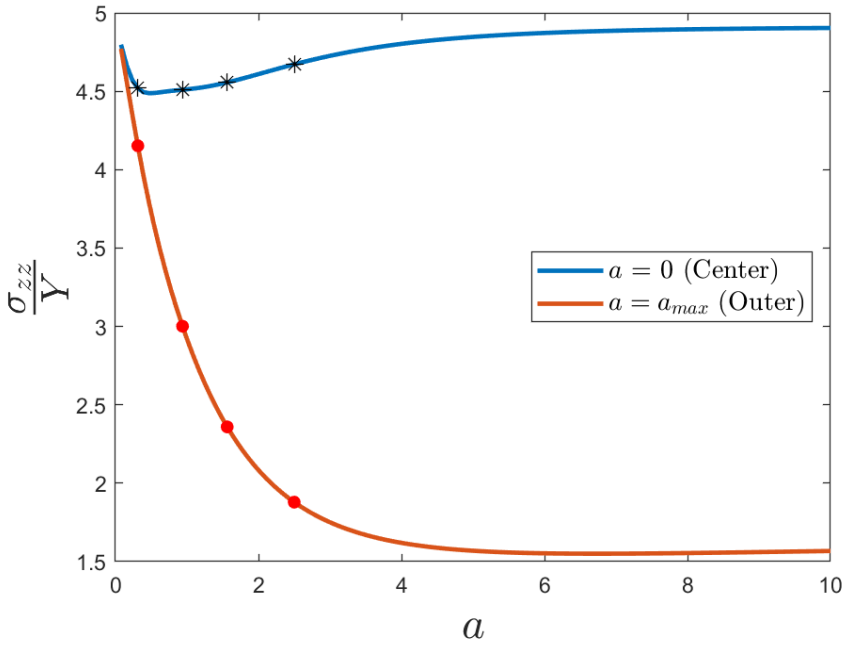

Figure 4-11: Stress in the vertical direction experienced by the shell at its center and exterior during the growth process ($A\tau + R_i$, $A = 0.1$, $R_i = H$, $a_{max} = 10$)

vertical directions. Interestingly, the value of σ_{zz} at the center of the shell is non-monotonic, initially showing some relaxation before gradually increasing. The normal stress in the vertical direction at the outermost edge of the shell sharply decreases as the shell bends. Once the shell reaches a certain aspect ratio ($a = 6$) both the deformation and the stress experienced by the shell remain unchanged as the shell continues to grow in the radial direction. Thus, the shell is only able to bend and relax the vertical stress to a certain amount.

Chapter 5

Conclusions and Future Work

5.1 Conclusions

With the kinematics of the shell outlined, the numerical method for solving the resulting boundary-value problem described, and the resulting solutions from multiple incompatible growth cases analyzed, we can now return to our problem statement for this thesis. The first item that we aimed to both measure and discuss was the influence of incompatibility on the shape of shell surface growth. Although we were only using arbitrary kinematic inputs to our model, the introduction of incompatibility drastically affected the shape of the shell. For the compatible growth case, the shell was able to grow uninhibited in the radial direction and each ring added to the shell did not experience any deformation in the radial or vertical direction. For the tensile incompatible growth case ($R' > 1$), the shell was stretched in the radial direction, and as a result was thinner than its original thickness in the vertical direction. The shell did not show a significant degree of bending. For the compressive growth case ($R' < 1$), the shell displayed a large degree of bending that originated at the early stages of the shell growth, i.e. when it had a sufficiently small aspect ratio of length over height. The compressive incompatibility between the rings influenced the shell to grow diagonally in both the radial and vertical directions.

The second goal of this project was to predict the role of the internal stresses of the growing shell and to track their development over time. While analyzing the

compressive incompatible growth case, we found compressive incompatibility leads to a large tensile stress in the vertical direction even at the early stages of shell growth. This normal stress in the vertical direction, σ_{zz}, is the root cause of the shape changes undergone by the shell for this growth case. In an effort to relax this stress, the shell reorients by bending and grows in both the radial and vertical directions. This stress relaxation seemingly dictates the shape of the shell up to a certain shell length, at which point the amount of stress that can be relaxed hits a limit and the angle at which rings are added to the shell remains constant.

This analysis of the stress in the shell ties into our third goal for the project - to draw conclusions about whether incompatibility can explain the crystallographic orientation obseved in seashell. While this can not be said with complete certainty, these results produced by our model do show that significant residual stresses are introduced into the shell by incompatible growth. These internal stresses largely affect the early stages of our shell's development and thus could explain the reorientation of the material internal structure seen in seashells.

5.2 Future Work

While the kinematic model, numerical method, and results presented in this paper are notable, there is much work to be done on this project in the future. The major avenue to improve this work is to develop the kinetic model for the growth of the limpet seashell. Rather than have the incompatibility prescribed by an arbitrary kinematic input decided by the user, the growth would be driven by a driving force similar to the one outlined by Abi-Akl et. al. [1]. This driving force would provide a fully coupled feedback loop between the kinematics and the kinetics of the shell surface growth model.

Another potential area for improvement for the model would be to add layers over time in the vertical direction in addition to the surface growth of a shell in the radial direction. As can be seen in Figure 1-3, the elongation of the lathes of the shell is the fastest growing front, but over a slower time new lathes do appear in the shell.

Our model currently simplifies the growth of the shell by only modeling the lathe elongation. To model the appearance of new lathes, future work could add additional layers in the vertical direction, allowing the parameter that controls the initial height (thickness) of a shell, H, to change as a function of time ($H(\tau)$), or have the thickness of the shell be dictated by the kinetic input to the system ($H(R(\tau))$).

Finally, another future goal of the project is to allow for the rings added to the shell to change their material properties over time. In the seashell, it is presumed that although the rings in the region near the nucleation site are softer and fully deformable, the "older" rings outside this region have stiffened, and are thus more accurately approximated as a rigid body. Adding this feature into the model would likely impact the boundary conditions presented in this thesis.

Appendix A

Coefficient Lookup

$$A_1(\tau) = -\frac{4H^3R'^2\left(3R'+1\right)}{45R^4} + \frac{2H^3\left(6R'+1\right)R''}{45R^3} + \frac{H\left(-2H^2R^{(3)}+5R'+10\right)}{45R^2} + \frac{1}{3H} \tag{A.1}$$

$$B_1(\tau) = -\frac{H^3R'^2\left(3R'+1\right)}{20R^4} + \frac{H^3\left(6R'+1\right)R''}{40R^3} - \frac{H\left(9H^2R^{(3)}-20R'-40\right)}{360R^2} - \frac{1}{3H} \tag{A.2}$$

$$C_1(\tau) = 0 \tag{A.3}$$

$$D_1(\tau) = \frac{4H^3R'\left(3R'+1\right)}{45R^3} - \frac{2H^3R''}{15R^2} \tag{A.4}$$

$$E_1(\tau) = \frac{H^3R'\left(3R'+1\right)}{20R^3} - \frac{3H^3R''}{40R^2} \tag{A.5}$$

$$F_1(\tau) = 0 \tag{A.6}$$

$$G_1(\tau) = -\frac{2H^3\left(3R'+1\right)}{45R^2} - \frac{2H}{9} \tag{A.7}$$

$$H_1(\tau) = -\frac{H^3\left(3R'+1\right)}{40R^2} - \frac{H}{9} \tag{A.8}$$

$$I_1(\tau) = \frac{H^2}{9R} \tag{A.9}$$

$$J_1(\tau) = 0 \tag{A.10}$$

$$K_1(\tau) = 0 \tag{A.11}$$

$$L_1(\tau) = -\frac{H^2}{9} \tag{A.12}$$

$$M_1(\tau) = \frac{2H^3}{45} \tag{A.13}$$

$$N_1(\tau) = \frac{H^3}{40} \tag{A.14}$$

$$Z_1(\tau) = -\frac{H(R' - R'^2 + R'R'')}{6RR'^2} \tag{A.15}$$

$$\begin{aligned} A_2(\tau) = &-\frac{H^3 R'^2 (3R' + 1)}{20R^4} + \frac{H^3 (6R' + 1) R''}{40R^3} \\ &- \frac{H \left(9H^2 R^{(3)} - 20R' - 40\right)}{360R^2} - \frac{1}{3H} \end{aligned} \tag{A.16}$$

$$\begin{aligned} B_2(\tau) = &-\frac{H^3 R'^2 (3R' + 1)}{30R^4} + \frac{H^3 (6R' + 1) R''}{60R^3} \\ &- \frac{H \left(6H^2 R^{(3)} - 40R' - 80\right)}{360R^2} + \frac{1}{3H} \end{aligned} \tag{A.17}$$

$$C_2(\tau) = 0 \tag{A.18}$$

$$D_2(\tau) = \frac{H^3 R' (3R' + 1)}{20R^3} - \frac{3H^3 R''}{40R^2} \tag{A.19}$$

$$E_2(\tau) = \frac{H^3 R' (3R' + 1)}{30R^3} - \frac{H^3 R''}{20R^2} \tag{A.20}$$

$$F_2(\tau) = 0 \tag{A.21}$$

$$G_2(\tau) = -\frac{H^3 (9R' + 3)}{120R^2} - \frac{H}{9} \tag{A.22}$$

$$H_2(\tau) = -\frac{H^3\,(6R' + 2)}{120R^2} - \frac{2H}{9} \tag{A.23}$$

$$I_2(\tau) = \frac{H^2}{18R} \tag{A.24}$$

$$J_2(\tau) = 0 \tag{A.25}$$

$$K_2(\tau) = 0 \tag{A.26}$$

$$L_2(\tau) = -\frac{H^2}{18} \tag{A.27}$$

$$M_2(\tau) = \frac{H^3}{40} \tag{A.28}$$

$$N_2(\tau) = \frac{H^3}{60} \tag{A.29}$$

$$Z_2(\tau) = -\frac{H(R' - R'^2 + R'R'')}{6RR'^2} \tag{A.30}$$

$$A_3(\tau) = -\frac{H^2R^{(3)}}{9R^2} - \frac{2H^2R'^3}{3R^4} + \frac{2H^2R'R''}{3R^3} \tag{A.31}$$

$$B_3(\tau) = -\frac{H^2R^{(3)}}{18R^2} - \frac{H^2R'^3}{3R^4} + \frac{H^2R'R''}{3R^3} \tag{A.32}$$

$$C_3(\tau) = 0 \tag{A.33}$$

$$D_3(\tau) = \frac{2H^2R'^2}{3R^3} - \frac{H^2R''}{3R^2} \tag{A.34}$$

$$E_3(\tau) = \frac{H^2R'^2}{3R^3} - \frac{H^2R''}{6R^2} \tag{A.35}$$

$$F_3(\tau) = 0 \tag{A.36}$$

$$G_3(\tau) = -\frac{H^2R'}{3R^2} \tag{A.37}$$

$$H_3(\tau) = -\frac{H^2 R'}{6R^2} \tag{A.38}$$

$$I_3(\tau) = 0 \tag{A.39}$$

$$J_3(\tau) = \frac{H^2}{9R} \tag{A.40}$$

$$K_3(\tau) = \frac{H^2}{18R} \tag{A.41}$$

$$L_3(\tau) = -\frac{H}{3} \tag{A.42}$$

$$M_3(\tau) = \frac{H^2}{9} \tag{A.43}$$

$$N_3(\tau) = \frac{H^2}{18} \tag{A.44}$$

$$Z_3(\tau) = 0 \tag{A.45}$$

Bibliography

[1] Rami Abi-Akl, Rohan Abeyaratne, and Tal Cohen. Kinetics of surface growth with coupled diffusion and the emergence of a universal growth path. *Proceedings of the Royal Society A*, 475(2221):20180465, 2019.

[2] D Ambrosi, Gerard A Ateshian, Ellen M Arruda, SC Cowin, J Dumais, A Goriely, Gerhard A Holzapfel, Jay D Humphrey, R Kemkemer, Ellen Kuhl, et al. Perspectives on biological growth and remodeling. *Journal of the Mechanics and Physics of Solids*, 59(4):863–883, 2011.

[3] D Ambrosi, A Guillou, and ES Di Martino. Stress-modulated remodeling of a non-homogeneous body. *Biomechanics and modeling in mechanobiology*, 7:63–76, 2008.

[4] Robert R Archer. *Growth stresses and strains in trees*, volume 3. Springer Science & Business Media, 2013.

[5] Bernd Bayerlein, Paul Zaslansky, Yannicke Dauphin, Alexander Rack, Peter Fratzl, and Igor Zlotnikov. Self-similar mesostructure evolution of the growing mollusc shell reminiscent of thermodynamically driven grain growth. *Nature Materials*, 13(12):1102–1107, 2014.

[6] CB Brown and LE0124 Goodman. Gravitational stresses in accreted bodies. *Proceedings of the Royal Society of London. Series A. Mathematical and Physical Sciences*, 276(1367):571–576, 1963.

[7] Kenneth M Brown and Charles Lydeard. Mollusca: gastropoda. In *Ecology and classification of North American freshwater invertebrates*, pages 277–306. Elsevier, 2010.

[8] Régis Chirat, Alain Goriely, and Derek E Moulton. The physical basis of mollusk shell chiral coiling. *Proceedings of the National Academy of Sciences*, 118(48):e2109210118, 2021.

[9] Régis Chirat, Derek E Moulton, and Alain Goriely. Mechanical basis of morphogenesis and convergent evolution of spiny seashells. *Proceedings of the National Academy of Sciences*, 110(15):6015–6020, 2013.

[10] Tal Cohen, Chon U Chan, and L Mahadevan. Competing failure modes in finite adhesive pads. *Soft matter*, 14(10):1771–1779, 2018.

[11] Susan D Day, P Eric Wiseman, Sarah B Dickinson, and J Roger Harris. Contemporary concepts of root system architecture of urban trees. *Arboriculture & Urban Forestry*, 36(4):149–159, 2010.

[12] Jacques Dumais and Dorota Kwiatkowska. Analysis of surface growth in shoot apices. *The Plant Journal*, 31(2):229–241, 2002.

[13] Krishna Garikipati, Ellen M Arruda, Karl Grosh, Harish Narayanan, and Sarah Calve. A continuum treatment of growth in biological tissue: the coupling of mass transport and mechanics. *Journal of the Mechanics and Physics of Solids*, 52(7):1595–1625, 2004.

[14] Alain Goriely. *The mathematics and mechanics of biological growth*, volume 45. Springer, 2017.

[15] Alain Goriely and Martine Ben Amar. On the definition and modeling of incremental, cumulative, and continuous growth laws in morphoelasticity. *Biomechanics and modeling in mechanobiology*, 6(5):289–296, 2007.

[16] Elizabeth Gosling. *Marine Mussels: Ecology, Physiology, Genetics and Culture*. John Wiley & Sons, 2021.

[17] Fabian Heinemann, Malte Launspach, Katharina Gries, and Monika Fritz. Gastropod nacre: structure, properties and growth—biological, chemical and physical basics. *Biophysical chemistry*, 153(2-3):126–153, 2011.

[18] Robinson Julie and C Kirt. International space station benefits for humanity, 2018.

[19] Jon Kadish, JR Barber, and PD Washabaugh. Stresses in rotating spheres grown by accretion. *International journal of solids and structures*, 42(20):5322–5334, 2005.

[20] Jon Kadish, JR Barber, PD Washabaugh, and Daniel J Scheeres. Stresses in accreted planetary bodies. *International Journal of Solids and Structures*, 45(2):540–550, 2008.

[21] Ellen Kuhl. Growing matter: a review of growth in living systems. *Journal of the Mechanical Behavior of Biomedical Materials*, 29:529–543, 2014.

[22] Jian Li, Mrityunjay Kothari, S Chockalingam, Thomas Henzel, Qiuting Zhang, Xuanhe Li, Jing Yan, and Tal Cohen. Nonlinear inclusion theory with application to the growth and morphogenesis of a confined body. *Journal of the Mechanics and Physics of Solids*, 159:104709, 2022.

[23] Vlado A Lubarda and Anne Hoger. On the mechanics of solids with a growing mass. *International journal of solids and structures*, 39(18):4627–4664, 2002.

[24] Mathworks. bvp4c (solve boundary value problem — fourth-order method). https://www.mathworks.com/help/matlab/ref/bvp4c.html, 2023. Accessed: 2023-04-28.

[25] Derek E Moulton and Alain Goriely. Surface growth kinematics via local curve evolution. *Journal of mathematical biology*, 68:81–108, 2014.

[26] Derek E Moulton, Alain Goriely, and Régis Chirat. Mechanical growth and morphogenesis of seashells. *Journal of theoretical biology*, 311:69–79, 2012.

[27] S Kiana Naghibzadeh, Noel Walkington, and Kaushik Dayal. Surface growth in deformable solids using an eulerian formulation. *Journal of the Mechanics and Physics of Solids*, 154:104499, 2021.

[28] Minnesota Department of Natural Resources. Adopt-a-river program - peanut. https://www.dnr.state.mn.us/adoptriver/peanut.html, 2013. Accessed: 2023-04-30.

[29] TB Randrup, EG McPherson, and LR Costello. A review of tree root conflicts with sidewalks, curbs, and roads. *Urban Ecosystems*, 5:209–225, 2001.

[30] Edward K Rodriguez, Anne Hoger, and Andrew D McCulloch. Stress-dependent finite growth in soft elastic tissues. *Journal of biomechanics*, 27(4):455–467, 1994.

[31] Vanessa Schoeppler, Robert Lemanis, Elke Reich, Tamás Pusztai, László Gránásy, and Igor Zlotnikov. Crystal growth kinetics as an architectural constraint on the evolution of molluscan shells. *Proceedings of the National Academy of Sciences*, 116(41):20388–20397, 2019.

[32] Vanessa Schoeppler, Deborah Stier, Richard J Best, Chengyu Song, John Turner, Benjamin H Savitzky, Colin Ophus, Matthew A Marcus, Shiteng Zhao, Karen Bustillo, et al. Crystallization by amorphous particle attachment: On the evolution of texture. *Advanced Materials*, 33(37):2101358, 2021.

[33] Hervey Woodburn Shimer. *An Introduction to the Study of Fossils (plants and Animals)*. Macmillan, 1914.

[34] R Skalak, DA Farrow, and A14782930883 Hoger. Kinematics of surface growth. *Journal of mathematical biology*, 35(8):869–907, 1997.

[35] Richard Skalak, G Dasgupta, M Moss, E Otten, P Dullemeijer, and H Vilmann. Analytical description of growth. *Journal of theoretical biology*, 94(3):555–577, 1982.

[36] Mariya Stavnichuk, Nicholas Mikolajewicz, Tatsuya Corlett, Martin Morris, and Svetlana V Komarova. A systematic review and meta-analysis of bone loss in space travelers. *npj Microgravity*, 6(1):13, 2020.

[37] Larry A Taber. Biomechanics of growth, remodeling, and morphogenesis. *Applied Mechanics Reviews*, 1995.

[38] Larry A Taber and Jay D Humphrey. Stress-modulated growth, residual stress, and vascular heterogeneity. *J. Biomech. Eng.*, 123(6):528–535, 2001.

[39] James B Thompson, George T Paloczi, Johannes H Kindt, Martina Michenfelder, Bettye L Smith, Galen Stucky, Daniel E Morse, and Paul K Hansma. Direct observation of the transition from calcite to aragonite growth as induced by abalone shell proteins. *Biophysical Journal*, 79(6):3307–3312, 2000.

[40] Laura Treccani, Karlheinz Mann, Fabian Heinemann, and Monika Fritz. Perlwapin, an abalone nacre protein with three four-disulfide core (whey acidic protein) domains, inhibits the growth of calcium carbonate crystals. *Biophysical journal*, 91(7):2601–2608, 2006.

[41] Russell T Turner. Invited review: what do we know about the effects of spaceflight on bone? *Journal of applied physiology*, 89(2):840–847, 2000.

[42] Loic Vanel, Daniel Howell, D Clark, RP Behringer, and Eric Clément. Memories in sand: Experimental tests of construction history on stress distributions under sandpiles. *Physical Review E*, 60(5):R5040, 1999.

[43] Chien M Wang. Timoshenko beam-bending solutions in terms of euler-bernoulli solutions. *Journal of engineering mechanics*, 121(6):763–765, 1995.

[44] Shitao Wu, Chang-Yang Chiang, and Wuzong Zhou. Formation mechanism of caco3 spherulites in the myostracum layer of limpet shells. *Crystals*, 7(10):319, 2017.

[45] Zhehan Ying, Shi Wang, Wai Chuen Wong, Xiangbin Cai, Xuemeng Feng, Shengling Xiang, Yuan Cai, Pei-Yuan Qian, and Ning Wang. An insight into the microstructures and composition of 2,700 m-depth deep-sea limpet shells. *Frontiers in Marine Science*, 9:902815, 2022.

[46] Domenico Zaza, Michele Ciavarella, and Giuseppe Zurlo. Strain incompatibility as a source of residual stress in welding and additive manufacturing. *European Journal of Mechanics-A/Solids*, 85:104147, 2021.

[47] Irena Žmak, Suzana Jakovljević, and Marija Bernat. Comparison of microstructure of the adriatic monodonta and the mediterranean limpet. *Matrib 2015. Materials, Wear, Recycling*, pages 407–417, 2015.